# Fractal Diffusion in High Temperature Polymer Electrolyte Fuel Cell Membranes

Bernhard Hopfenmüller,[1] Reiner Zorn,[2] Olaf Holderer,[1] Oxana Ivanova,[1] Werner Lehnert,[3,4] Wiebke Lüke,[3] Georg Ehlers,[5] Niina Jalarvo,[6,7] Gerald J. Schneider,[8] Michael Monkenbusch,[2] and Dieter Richter[2]
[1] *Forschungszentrum Jülich GmbH, Jülich Centre for Neutron Science at Heinz Maier-Leibnitz Zentrum (MLZ), 85747 Garching, Germany*
[2] *Forschungszentrum Jülich GmbH, Jülich Centre for Neutron Science (JCNS-1) and Institute for Complex Systems (ICS-1), 52425 Jülich, Germany*[a]
[3] *Forschungszentrum Jülich GmbH, Institute of Energy and Climate Research (IEK-3): Electrochemical Process Engineering, 52425 Germany*
[4] *RWTH Aachen University, Faculty of Mechanical Engineering, Germany*
[5] *Neutron Technologies Division, Oak Ridge National Laboratory, Oak Ridge, TN 37831-6475, USA*
[6] *Jülich Centre for Neutron Science, Oak Ridge National Laboratory, Oak Ridge, Tennessee 37831, USA*
[7] *Neutron Scattering Division, Oak Ridge National Laboratory, Oak Ridge, TN 37831-6473, USA*
[8] *Department of Chemistry and Department of Physics, Louisiana State University, Baton Rouge, LA 70803, USA*

(Dated: 10 May 2018)

The performance of fuel cells depends largely on the proton diffusion in the proton conducting membrane, the core of a fuel cell. High temperature polymer electrolyte fuel cells (HT-PEFCs) are based on a polymer membrane swollen with phosphoric acid as the electrolyte, where proton conduction takes place. We studied the proton diffusion in such membranes with neutron scattering techniques which are especially sensitive to the proton contribution. Time of flight spectroscopy and backscattering spectroscopy have been combined to cover a broad dynamic range. In order to selectively observe the diffusion of protons potentially contributing to the ion conductivity, two samples were prepared, where in one of the samples the phosphoric acid was used with hydrogen replaced by deuterium. The scattering data from the two samples were subtracted in a suitable way after measurement. Thereby subdiffusive behavior of the proton diffusion has been observed and interpreted in terms of a model of fractal diffusion. For this purpose, a scattering function for fractal diffusion has been developed. The fractal diffusion dimension $d_w$ and the Hausdorff dimension $d_f$ have been determined on the length scales covered in the neutron scattering experiments.

## I. INTRODUCTION

In the modern world alternatives to fossil fuels are crucial. For example in the automotive sector hydrogen powered fuel cells provide a reasonable and worthwhile alternative to fossil fuel powered internal combustion engines. Usually in fuel cell driven cars, Polymer Electrolyte Fuel Cells (PEFC) are used[1,2]. The most common commercially available and prominent material for the electrolyte membrane is Nafion. But also fuel cells for small to medium stationary applications or Auxiliary Power Units (APUs) are under development, one example being the High Temperature Polymer Electrolyte Fuel cell (HT-PEFC)[3].

The proton conductivity depends on the water content of the membrane. Therefore the operating temperature at ambient pressure for Nafion-based membranes is limited to temperatures below 100 °C. If operating temperatures well above 100 °C are required, perfluorinated proton exchange membranes are not suitable and alternative materials come into play. The most prominent material class for operating temperatures up to 180 °C in the so-called High-temperature Polymer Electrolyte Fuel Cell (HT-PEFC) are polybenzimidazole (PBI) type polymers. These polymers do not have any intrinsic proton conductivity but are able to take up a high amount of phosphoric acid, which provides the required ionic conductivity of the membrane. Poly[2,2‘-(m-phenylene)-5,5‘-bibenzimidazole (*m*PBI) membranes were first synthesised in the 1960ies[4] with the objective to obtain a material for aerospace applications, durable at high thermal stress. Since the late 1990ies PBI membranes are used for HT-PEFC applications[5,6]. Meanwhile, many different copolymers of benzimidazole have been synthesized[7]. For example, an alternative membrane material for such high operating temperatures is ABPBI. The monomeric units of ABPBI and *m*PBI differ in an additional benzene ring for every two benzimidazole groups in the latter (Fig. 1). Further modifications of PBI type polymers are introduced by crosslinking and/or plasticizing. In our study we use a PBI derivative optimized in this way for industrial applications.

A valuable tool to investigate structural and dynamic features of these proton conducting membranes is neu-

---

[a] Electronic mail: r.zorn@fz-juelich.de

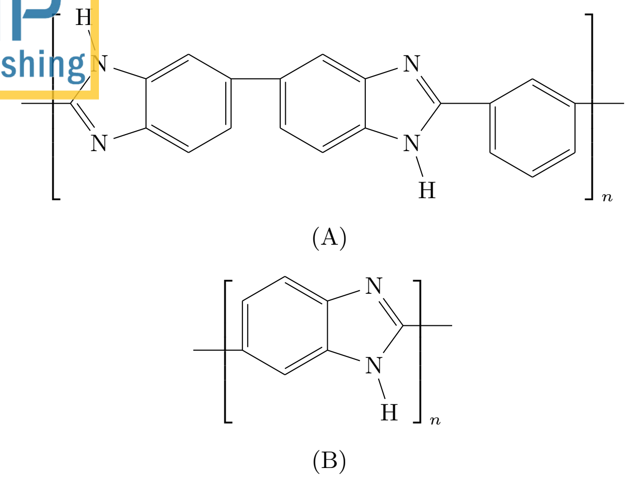

(A)

(B)

FIG. 1. Monomeric units of *m*PBI (A) and ABPBI (B).

tron scattering. Neutron scattering is a noninvasive technique and allows in the ideal case an in-situ and in-operando investigation of hydrogen or deuterium containing systems. Hydrogen and its isotope Deuterium have significantly different interaction strengths with neutrons, while providing similar chemical features. Thus, by deuterating, i.e. replacing hydrogen with deuterium, one can separate signals of multi-component systems and study them still at the same time. The structural features and the dynamic processes of Nafion-based systems has been issue of (neutron ) scattering for the last 30 years, e.g. in ref. 8–18. Starting from the first proposal of a micella-like structure of Nafion systems[9], consecutive investigations[10,11,13] could disprove those findings.

Volino et al. carried out first quasi-elastic neutron scattering (QENS) experiments for dynamic investigations[19] on PEFC membranes, namely on Nafion membranes. Their findings describe the dynamics as diffusion in a sphere on short length scales[8]. In a later work[15,16] from the same group the sphere is considered as a polymer-water mixture with a Gaussian concentration profile of water[14]. This change of the model actually leads to a simplification of the mathematics while preserving the feature of a limited diffusion range. Pivovar et al.[12] combine the original model of a continuous diffusion in a sphere with jump diffusion of Hall-Ross-type[20]. Very recently, a dependence of the diffusion coefficient on length scale was detected by comparison of QENS and pulsed field gradient (PFG) NMR[21]. From this experimental finding and accompanying molecular dynamics (MD) simulation, the authors conclude that the underlying dynamics is subdiffusive.

While Nafion-based systems are already thoroughly investigated, the understanding of PBI-based systems is much more limited. Although the macroscopic features of *m*PBI and ABPBI systems are well studied (eg.[22,23]), the microscopic processes are not understood in full detail. Prior neutron scattering studies of PBI-based systems were mainly based on imaging[24,25]. In first quasielastic neutron scattering studies we could observe the temperature dependence of the dynamical processes in these materials[26]. Further we could demonstrate fractal structures in ABPBI (Fig. 1(b)) membranes on nm length scales using small-angle neutron- and x-ray scattering (SANS, SAXS)[27].

In the present paper we wish to deepen the insight into the dynamics of protons in PBI-based PEFC membranes by a systematic study of the microscopic dynamic correlation function with quasielastic neutron scattering. In general, two fundamentally different mechanisms are possible for hydrogen diffusion in polymer membranes. The vehicle mechanism[28] that transports hydrogen atoms bound to larger carrier molecules, like e.g. $H_4PO_4^+$ or $H_3O^+$ and the Grotthuss mechanism transporting protons through a sequence of binding sites whose mobility is much smaller than that of the protons (figuratively often called "bucket brigade mechanism"). A detailed treatment of the two mechanisms, how they are realized microscopically, and in which systems they occur can be found in a review by Kreuer et al.[29]

Various authors[22,30,31] could show that for phosphoric-acid-doped PBI systems the Grotthuss mechanism is a relevant mechanism proton transport. E.g., in ref. 30 the main transport path is considered to be alongside the imide sites of the polymer chains assisted by a Grotthuss mechanism involving the phosphate ions. The dominance of structural diffusion could recently be confirmed by NMR measurements[32] although the latter authors conclude that the transport path is not involving the polymer. Interestingly, in that way the conduction mechanism differs fundamentally from that in 85 wt% phosphoric acid where the vehicle mechanism dominates[33]. The only work employing QENS on an unpolymerized benzimidazole system by now has been published by Melchior and Frick[34]. They could show with their most recent QENS-NMR experiments that the hydrogen bond network frustration reduces with increasing benzimidazole content via a decrease of the diffusion coefficient of protons in the nanosecond scale. They also showed that the intermolecular proton transfer is less likely to occur with higher benzimidazole content.

In our paper, we will present QENS results on commercial films of a PBI polymer soaked with phosphoric acid. We will first describe theory and methods used to obtain the data. Then we will discuss sample preparation and finally the results. Our first approach was to fit the data using an empirical Kohlrausch function. The individual fits were quite acceptable, but there were certain systematic deviations and the dependence of the characteristic relaxation time on the magnitude of the scattering vector $Q$ was not compatible with the Kohlrausch function resulting from a homogeneous process. This led us to attempt a description with a distribution of Debye like relaxations ensuing a heterogeneous picture. In this way the individual data could be described better, but the $Q$ dependence was again not the expected one. The fact, that in the low $Q$ range a power law $\tau \propto Q^{-n}$ was found with $n$ being inconsistent with both models, motivated a (third) description by fractal diffusion. This model was able to describe the data in the low $Q$ range simultaneously for all $Q$ values and temperatures $\geq 300$ K showing plausible results. It allows to draw a more concrete picture of the actual diffusion process.

## II. THEORY

### A. Theory of Inelastic Neutron Scattering

To explain the scattering theory of an inelastic experiment, we will start by assuming a system of $N$ atoms propagating in time, starting at $t = 0$. The probability density to find an atom after time $t$ at a distance $\mathbf{r}$ is given by the so called van Hove correlation function:

$$G(\mathbf{r},t) = \frac{1}{N}\left\langle \int d^3r' \sum_{i,j} \delta(\mathbf{r} - \mathbf{r}' + \mathbf{r}_j(t))\delta(\mathbf{r}' - \mathbf{r}_i(0)) \right\rangle \tag{1}$$

From (1) we can define the van Hove self correlation function which determines the probability to find an atom after a time $t$ in distance $\mathbf{r}$ from its position at time 0. To do so we set $i = j$:

$$G(\mathbf{r},t)_{\text{self}} = \frac{1}{N}\left\langle \int d^3r' \sum_{j} \delta(\mathbf{r} - \mathbf{r}' + \mathbf{r}_j(t))\delta(\mathbf{r}' - \mathbf{r}_j(0)) \right\rangle \tag{2}$$

Calculating a spatial Fourier transform of (1) and (2) gives the intermediate scattering functions:

$$I_{\text{coh}}(\mathbf{Q},t) = \frac{1}{N}\sum_i \sum_j \langle \exp\left[\text{i}\mathbf{Q}\cdot\mathbf{r}_i(t)\right] \exp\left[\text{-i}\mathbf{Q}\cdot\mathbf{r}_j(0)\right]\rangle \tag{3}$$

and

$$I_{\text{inc}}(\mathbf{Q},t) = \frac{1}{N}\sum_i \langle \exp\left[\text{i}\mathbf{Q}\cdot\mathbf{r}_i(t)\right] \exp\left[\text{-i}\mathbf{Q}\cdot\mathbf{r}_i(0)\right]\rangle\,. \tag{4}$$

As indicated by the index, those functions correspond to the coherent and incoherent scattering. (3) describes scattering superposed from one particle at $t = 0$ and a second particle at a later time and is called the coherent scattering function. In contrast (4) describes the scattering superposed from one particle at time $t = 0$ and later time $t$. Backscattering and time-of-flight (TOF) experiments however deliver the scattering intensity in terms of energy $S(\mathbf{Q},\omega)$. This can be seen as the Fourier transform of the intermediate scattering functions:

$$S(\mathbf{Q},\omega) = \frac{1}{2\pi}\int_{-\infty}^{\infty} I(\mathbf{Q},t)\exp\left[-\text{i}\omega t\right]\text{d}t. \tag{5}$$

### B. Data treatment

#### 1. Fourier transform

Generally the treatment of data in time domain is motivated by the different energy resolutions that spectrometers offer. Therefore it is a common approach to combine data from TOF and back-scattering by using a numerical Fourier transform:

$$I(\mathbf{Q},t) = \int_{-\infty}^{\infty} S(\mathbf{Q},\omega)\exp\left[i\omega t\right]\text{d}\omega. \tag{6}$$

The measured scattering function is a convolution of the ideal scattering function $S(\mathbf{Q},\omega)$ and the instrumental resolution function $R(\mathbf{Q},\omega)$:

$$\tilde{S}(\mathbf{Q},\omega) = S(\mathbf{Q},\omega)\otimes R(\mathbf{Q},\omega) \tag{7}$$

According to the Convolution theorem (7) becomes a product after Fourier transform:

$$\tilde{I}(\mathbf{Q},t) = S(\mathbf{Q},t)R(\mathbf{Q},t) \tag{8}$$

To obtain the pure scattering function we need to divide the Fourier-transformed measured scattering function $\tilde{I}(\mathbf{Q},t)$ by the resolution function. For an estimation of the latter we measured the sample at 3K. For such low temperatures one can exclude inelastic scattering contributions aside from zero point vibrations. Finally one gets:

$$\frac{I(\mathbf{Q},t)}{S(\mathbf{Q})} = \frac{\mathcal{F}\{\tilde{S}(\mathbf{Q},\omega)\}}{\mathcal{F}\{R(\mathbf{Q},\omega)\}} = \frac{\tilde{I}(\mathbf{Q},t)}{R'(\mathbf{Q},t)}, \tag{9}$$

with $R'(\mathbf{Q},t)$ being the measured resolution. It is important to understand that the $Q$ dependence of coherent scattering intensity gets fully lost in this step if the resolution is obtained from a low temperature measurement of the sample itself (as done here) and $S(\mathbf{Q})$ has negligible temperature dependence. That is indicated here by the left site of the equation 9. Strictly one would have to indicate that explicitly for any further formulations of the scattering function. However, we will only point it out here and use $S(\mathbf{Q},\omega)$ and $I(\mathbf{Q},t)$ in the following.

#### 2. Data subtraction

The goal of the scattering experiments was to observe the hydrogen diffusion underlying the ionic conduction relevant for fuel cell applications. To this end, it is important to recognize that in a neutron scattering experiment all hydrogen nuclei contribute equally to the total scattering. Therefore, it is desirable to separate the contribution of the protons which are able to contribute to a (long range) diffusion from that of the protons in hydrogen atoms which are covalently bound to the polymer chain. Apart from the protons in low-molecular species (phosphoric acid, water) also protons bound to the imine groups in the polymer chain fall into the first category of 'mobile' protons because they may exchange with the former. For that reason, we aimed at preparing a sample with fully deuterated phosphoric acid $D_3PO_4$ of same concentration. By subtracting the scattering data of such a sample from that of a non-deuterated sample, one remains in the end with the incoherent scattering of 'mobile' protons only.

To understand the subtraction we take a look at the scattering data in the in the form of an 'effective total' $S(\mathbf{Q},\omega)$ presented by most neutron scattering data reduction software, e.g. INX[35]:

$$S(\mathbf{Q},\omega) = \frac{\sum_{k=1}^{m} n_k \sigma_k S_k(\mathbf{Q},\omega)}{\sum_{k=1}^{m} n_k \sigma_k} \tag{10}$$

$k$ is the index for the different sorts of atoms, present in a sample. $\sigma_k$ is the total neutron scattering cross section. $S_k(\mathbf{Q},\omega)$ is the partial scattering function of one sort of atoms. Strictly speaking, this expression is valid only for incoherent scattering or in the high $Q$ limit. But because the major contribution here *is* incoherent scattering from hydrogen we consider this approximation sufficient. With "sort" we mean the set of atoms giving rise to the same partial structure factor either by identical positions in the polymer chain or because they can exchange. In that sense, the hydrogen atoms in water, phosphoric acid, and those bound to the imidazole group belong to one sort because they can interchange by acid-base reactions on time scales much shorter than the duration of the neutron scattering experiments. Because these are also the only hydrogen atoms which are mobile over long ranges and can give rise to proton conductivity they are denoted by $\mathrm{H_{mob}}$. Because of the linearity of the Fourier transform the same relation holds for $S(\mathbf{Q},\omega)$ replaced by $I(\mathbf{Q},t)$. Actually the subtraction was performed after Fourier transform. Therefore, the version in time domain will be used from here on.

For the fully protonated sample (10) becomes:

$$I_\mathrm{h}(\mathbf{Q},t) = \frac{n_{\mathrm{H_{mob}}}\sigma_\mathrm{H} I_{\mathrm{H_{mob}}}(\mathbf{Q},t) + \sum_{k=2}^{m} n_k\sigma_k I_k(\mathbf{Q},t)}{n_{\mathrm{H_{mob}}}\sigma_\mathrm{H} + \sum_{k=2}^{m} n_k\sigma_k}, \tag{11}$$

with $k = 1$ for the $\mathrm{H_{mob}}$ atoms. Analogously to this we can describe the deuterated sample:

$$I_\mathrm{d}(\mathbf{Q},t) = \frac{n_{\mathrm{D_{mob}}}\sigma_\mathrm{D} I_{\mathrm{H_{mob}}}(\mathbf{Q},t) + \sum_{k=2}^{m} n_k\sigma_k I_k(\mathbf{Q},t)}{n_{\mathrm{H_{mob}}}\sigma_\mathrm{D} + \sum_{k=2}^{m} n_k\sigma_k} \tag{12}$$

It should be mentioned that in the ideal case $n_{\mathrm{D_{mob}}} = n_{\mathrm{H_{mob}}}$ and the dynamics of hydrogen and deuterium ions are identical. Assuming that, we get the following expression for $I_{\mathrm{H_{mob}}}(\mathbf{Q},t)$:

$$\begin{aligned} I_{\mathrm{H_{mob}}}(\mathbf{Q},t) &= \frac{1}{n_{\mathrm{H_{mob}}}(\sigma_\mathrm{H}-\sigma_\mathrm{D})} \\ &\left(\left(n_{\mathrm{H_{mob}}}\sigma_\mathrm{H} + \sum_{k=2}^{m} n_k\sigma_k\right) I_\mathrm{h}(\mathbf{Q},t) - \right. \\ &\left.\left(n_{\mathrm{H_{mob}}}\sigma_\mathrm{D} + \sum_{k=2}^{m} n_k\sigma_k\right) I_\mathrm{d}(\mathbf{Q},t)\right) \end{aligned} \tag{13}$$

As it will be presented later (section III B), we did not achieve the ideal case $n_{\mathrm{D_{mob}}} = n_{\mathrm{H_{mob}}}$. To compensate that, we did not use the normal scattering cross section $\sigma$ for our calculation, rather the so-called macroscopic scattering cross section $\Sigma$:

$$\Sigma = \sigma\rho \tag{14}$$

where $\rho$ is the number density of scatterers.

In addition we took into account that $\Sigma(Q)$ depends on $Q$ due to coherent scattering contributions. $\Sigma_d(Q)$ was determined by DNS[36] at MLZ used as neutron diffractometer with polarization analysis. The corresponding measurement is shown in Fig.2. $\Sigma_h$ was taken to be constant in the whole $Q$ range because incoherent scattering dominates in the non-deuterated sample.

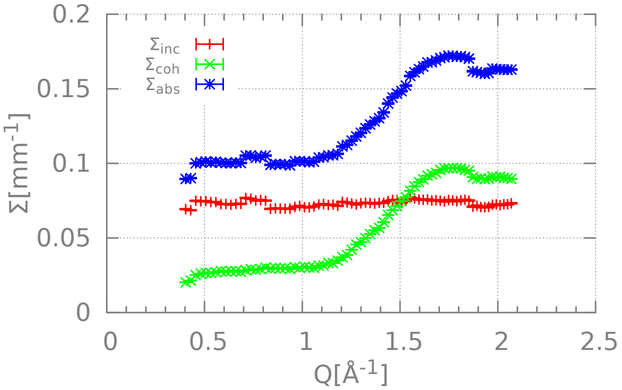

FIG. 2. $Q$ dependence of $\Sigma_d$ of the deuterated sample measured by DNS[36]. $\Sigma_\mathrm{tot} = \Sigma_d$ is the total macroscopic scattering cross section used in equation (15). $\Sigma_\mathrm{inc}$ and $\Sigma_\mathrm{coh}$ are the components identified as spin-incoherent and coherent/isotope-incoherent by the polarisation analysis on DNS.

Finally, the subtracted data was achieved in the following way:

$$I_{\mathrm{H_{mob}}}(\mathbf{Q},t) = \frac{\Sigma_h I_\mathrm{h}(\mathbf{Q},t) - \Sigma_d(\mathbf{Q}) I_\mathrm{d}(\mathbf{Q},t)}{\Sigma_h - \Sigma_d(\mathbf{Q})}. \tag{15}$$

## III. EXPERIMENTAL

### A. Neutron scattering

We used three different types of techniques, respectively instruments, to obtain the scattering data. The characteristics relevant for the data evaluation are summarized in table I.

1. Time-of-Flight Spectrometer CNCS at SNS[37]

   CNCS is a chopper-based direct geometry TOF spectrometer at the Spallation Neutron Source (SNS), Oak Ridge National Laboratory (ORNL). It was used with an incident wavelength of 4.9 Å resulting the resolution and $Q$-$\omega$ range stated in table I. The maximum energy transfer would be higher, but is restricted to the listed values due to kinematic constraints at the $Q$ values used.

2. Backscattering Spectrometer SPHERES at MLZ[38,39]

   SPHERES is a standard backscattering spectrometer deploying a phase space transformer to increase intensity at Maier-Leibnitz Zentrum (MLZ). Monochromator and analyzers are Si(111) resulting in a fixed wavelength of 6.27 Å and a resolution of 0.65 $\mu$eV. The maximum energy transfer $\pm 31$ $\mu$eV is limited by the speed of the Doppler drive.

3. Time-of-Flight Backscattering Spectrometer BASIS at SNS[40]

   BASIS is an inverse geometry TOF spectrometer at SNS, ORNL. The Si(111) analysers are in near-backscattering conditions yielding a resolution of 3.5 $\mu$eV at a wavelength of 6.27 Å. Due to frame overlap only the energy range $\pm 100\,\mu$eV could be used.

TABLE I. Overview of the inelastic neutron scattering instruments used. Dashes (—) indicate the ranges actually covered. Dots (. . . ) denote variable limits depending on $Q$.

| | CNCS | BASIS | SPHERES |
|---|---|---|---|
| $Q$ range [Å$^{-1}$] | 0.4—2.9 | 0.3—1.9 | 0.2—1.8 |
| energy resolution [$\mu$eV] | 100 | 3.5 | 0.65 |
| energy range [meV] | 2 . . . 10 | 0.1 | 0.029 |
| time range after FT [ps] | 0.1 . . . 1—40 | 10—800 | 50—3500 |

For all three instruments the same samples were used in the same containers. The containers had flat plane geometry. The thickness was chosen to be 0.2 mm for the protonated sample and 1.05 mm for the deuterated in order to obtain roughly 90% transmission for both samples. For the background correction an empty sample holder with the PFA protective foils only was measured at identical temperatures. To save measurement time, the background data was generated by interpolation for some temperatures. For the original normalization, a flat piece of vanadium was used. But it has to be noted that due to the later normalization with equation (9) the vanadium normalization is overridden.

By combining the three instruments, we could cover a time window from 0.1 ps (at high $Q$) to 3.5 ns after Fourier transform with considerable overlap between the instruments. It has to be noted, that this combination is only possible in the $Q$ range where data of all three instruments is available (0.3—1.8 Å$^{-1}$).

### B. Sample preparation

A crosslinked PBI (Fumapem AM-55, Lot Nr. 1759 1111)[41] was obtained from Fumatech BWT GmbH, Bietigheim-Bissingen, Germany in membrane sheets with a thickness of about 40 $\mu$m. It is the same material used in earlier studies[42]. After drying them in an ultra high vacuum, to get rid of unwanted synthesis waste-products, they were cut into pieces of desired size in inert gas atmosphere. The samples used for the data subtraction as described in subsection II B 2 were prepared with 85 wt% h- or d-phosphoric acid in $H_2O$ or $D_2O$ respectively. The phosphoric acids were purchased from Sigma Aldrich. The minimum degree of deuteration of the d-phosphoric acid was specified as 98% by the supplier. To avoid exchange of deuterium with hydrogen from atmospheric humidity, the membranes were handled in a glove box before and after doping in a closed vessel. The phosphoric acid content was determined from the weight increase of the membranes during the doping process and is a function of time of immersion of the membranes in phosphoric acid. Finally the single membrane pieces were stacked to get a useful thickness for achieving a reasonable scattering intensity. We tried to prepare samples swollen with with the same concentration of deuterated and protonated acid in order to do a subtraction as mentioned in section II B 2.

TABLE II. Overview of prepared samples

| sample # | acid content [wt%] | doping time [min] |
|---|---|---|
| 1 | 386 $H_3PO_4$ | 1040 |
| 2 | 558 $D_3PO_4$ | 1058 |

As Tab.II shows, it was quite challenging to achieve that. The doping process is not clearly predictable, but seems to depend highly on the individual sample. Presumably either doping with $D_3PO_4$ is favourable compared to $H_3PO_4$ or an unknown factor is involved in the doping process, that we cannot control yet. It would certainly be interesting to study this phenomenon further and produce a sample which is better matched. Nevertheless, we consider the use of data from the given sample for the subtraction to be better than doing no subtraction at all or using a dry membrane for the subtraction. In the latter case, although the total scattering from the polymer would be the same, the dynamics would be different because the polymer is in a different environment. Since the function of the phosphoric acid in the sample used for subtraction is only to provide such an environment, we do not assume that the difference in the acid contents induces a significant error in the subtracted data.

It has also to be noted that the composition of the phosphoric acid in the membrane is not identical to that in the doping bath[42]. According to ref. 42, at 386 wt% mass uptake, the concentration of the imbibed phosphoric acid would be 96–97%. As a caveat, we note that our way of preparation was not identical to the one used in that publication. Nevertheless, since the relation between total mass uptake and phosphoric acid content found was identical for different preparation protocols, we think that it is also a reasonable estimate for our samples. Notwithstanding the remaining uncertainty, the sample nonetheless represents a configuration close to the real conditions in a fuel cell with its dynamically varying water contents during operation. At that concentration a condensation of phosphoric acid to pyrophosphoric acid and higher polyphosphoric acids may take place. For pure phosphoric acid the fraction of phosphorous atoms in polyphosphoric acids should not exceed 5% at 400 K[32]. For nominally dry (100%) phosphoric acid mixed with benzimidazole, the fraction of polyphosphoric acids increases with temperature but stays below 11–13% for temperatures ≤ 430 K[33].

After doping, the samples were wrapped and heat-sealed in a commercial Perfluoroalkoxy alkane (PFA) -foil to prevent any interaction of acid with metallic surfaces or exchange of deuterium in the sample with hydrogen from atmospheric humidity. The flat-geometry sample holders for the scattering experiments were – after loading with the finished samples – sealed by welding.

## IV. RESULTS

### A. Empirical Approach

After subtraction, background correction of scattering contributions from the PFA foil and Fourier transform of the data as explained above, we chose a $Q$ value of 1.77 Å$^{-1}$ for a first temperature-dependent empirical approach with a simple stretched-exponential function. The utilization of this function, also known as Kohlrausch function[43], provides a simple and widely used approach to describe QENS-Data:

$$\Phi(t) = \exp\left[-\left(\frac{t}{\tau(Q,T)}\right)^{\beta}\right] \qquad (16)$$

Since the scattering data do not decay to zero for long times, equation (16) had to be modified by an Elastic Incoherent Scattering Factor (EISF):

$$I(Q,t) = A[(1 - EISF) \cdot \Phi(t) + EISF] \qquad (17)$$

The EISF describes the long-time spatial restriction of the motion, e.g. immobile protons in the system. The prefactor $A$ describes the damping amplitude, attributable to the Debye-Waller-Factor from motions and vibrations at short times. The rather high $Q$ value of 1.77 Å$^{-1}$ for the first fit approach was chosen for two reasons: On one hand multiple scattering effects are much less likely to contribute at higher $Q$ values and on the other hand only at high $Q$ values it is possible to observe the complete decay of $I(Q,t)$ to 0. The corresponding fit in Fig. 3 shows data in a temperature range from 240 K to 430 K at $Q = 1.77$ Å$^{-1}$ with an obtained stretching parameter $\beta = 0.42$. As it can be seen the Kohlrausch fit describes the data well for short times. However, for intermediate temperatures, where the tail of the relaxation is observable in the experimental time window, it becomes clear that the actual tail is more pronounced than that of the fit function.

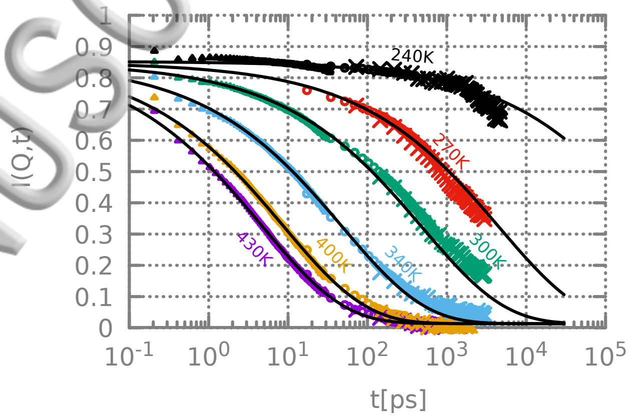

FIG. 3. Kohlrausch fit for QENS data at 1.77 Å$^{-1}$ in a temperature range from 240 K to 430 K. CNCS (△), BASIS (○) and SPHERES (✕). Temperatures are indicated by the labels next to the data (different colors of the symbols online). For CNCS and BASIS the error bars are smaller than the symbol size for SPHERES roughly the size of the symbol.

From $Q$-dependent fits (Fig. 4–6) we could obtain the spatial behavior of the characteristic relaxation time $\tau$. For the Kohlrausch function resulting from a homogeneous process $\tau \propto Q^{-2/\beta} = Q^{-4.8}$ is expected. However, we found that the $Q$ dependence is weaker, namely $\tau \propto Q^{-2.4\ldots2.8}$ (Fig. 7). This led us to a second (heterogeneous) approach based on an explicit distribution of relaxation times.

### B. Distribution of Relaxation Processes

Any completely monotonic relaxation function can be interpreted as arising from a distribution of Debye-like

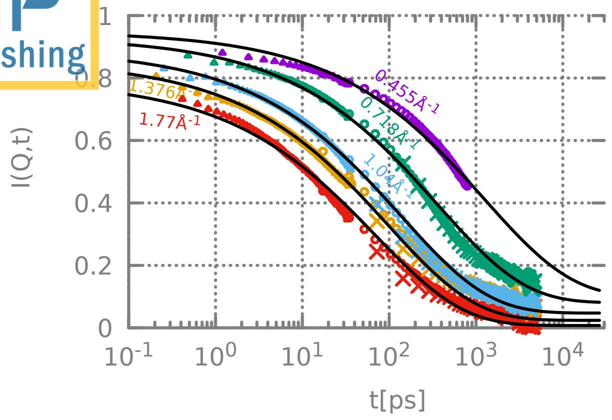

FIG. 4. Kohlrausch fit for QENS data at 340 K in a Q- range from 0.455 to 1.77 Å$^{-1}$. CNCS (△), BASIS (○) and SPHERES (×). $Q$ values are indicated by the labels next to the data (different colors of the symbols online). For CNCS and BASIS the error bars are smaller than the symbol size for SPHERES roughly the size of the symbol.

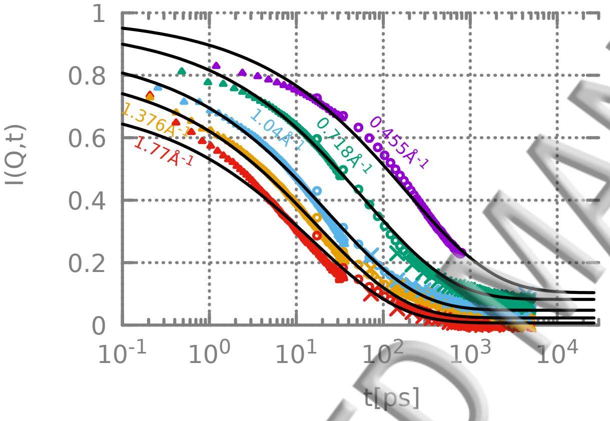

FIG. 5. Kohlrausch fit for QENS data at 400 K in a $Q$ range from 0.455 to 1.77 Å$^{-1}$. CNCS (△), BASIS (○) and SPHERES (×). $Q$ values are indicated by the labels next to the data (different colors of the symbols online). For CNCS and BASIS the error bars are smaller than the symbol size for SPHERES roughly the size of the symbol.

relaxations:

$$\Phi(t)=\int g(\ln\tau)\exp[-t/\tau]\mathrm{d}\ln\tau \tag{18}$$

Here we assume a Normal distribution of activation energies $g(E_a)$ due to a dynamic heterogeneity of the sample ensuing a log-Normal distribution of the corresponding relaxation times. $g(\ln\tau)$ is then of the form:

$$g(\ln\tau)=\frac{1}{\sqrt{2\pi}\sigma}\exp\left[-x^2\right], \tag{19}$$

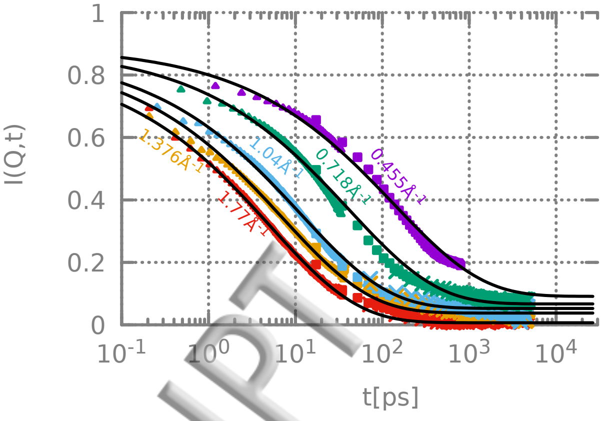

FIG. 6. Kohlrausch fit for QENS data at 430 K in a $Q$ range from 0.455 to 1.77 Å$^{-1}$. CNCS (△), BASIS (○) and SPHERES (×). $Q$ values are indicated by the labels next to the data (different colors of the symbols online). For CNCS and BASIS the error bars are smaller than the symbol size for SPHERES roughly the size of the symbol.

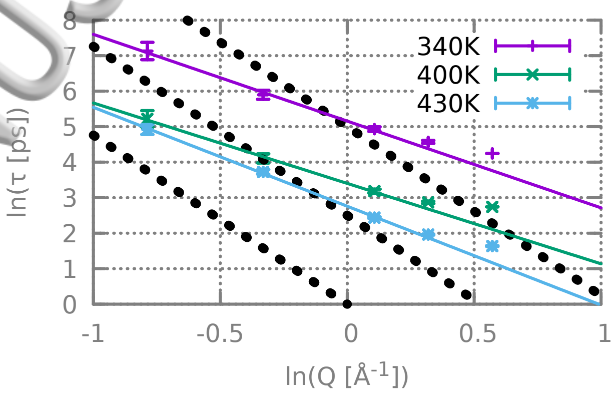

FIG. 7. $Q$ dependence of Kohlrausch relaxation times obtained from Fig. 4–6 The dotted lines correspond to $\tau \propto Q^{-2/\beta}$.

with

$$x=\frac{\ln(\tau/\tau_{\mathrm{avg}})}{\sqrt{2}\sigma}. \tag{20}$$

The corresponding intermediate scattering function can be calculated as:

$$\Phi(t)=\frac{\sqrt{2}\sigma}{\pi}\int_{-\infty}^{\infty}\mathrm{d}x\exp\left[-x^2\right]\exp\left[\frac{-t}{\tau_{\mathrm{avg}}\exp\left[\sqrt{2}\sigma x\right]}\right]. \tag{21}$$

More details are to be found in the supplementary materials. The temperature-dependent fitting parameters are then the average (more precisely: geometric mean) relaxation time $\tau_{\mathrm{avg}}$ for one temperature and the width $\sigma$.

For low temperatures one can see an additional relaxation process at short times, possibly attributable to a jump-rotation of hydrogen on suitable oxygen-sites of a phosphate ion:

$$I_{\text{rot}}(Q,t) = f_r(1-EISF_{\text{rot}})\exp\left[-\frac{t}{\tau_{\text{rot}}}\right] + 1 - f_r\left(1-EISF_{\text{rot}}\right) \qquad (22)$$

Since this process is temperature activated, the relaxation time $\tau_{\text{rot}}$ was described by an Arrhenius behavior:

$$\tau_{\text{rot}} = \tau' \exp\left[\frac{E}{k_B T}\right] \qquad (23)$$

$\tau'$ was found to be stable at 0.03 ps. In all subsequent fits it was fixed at that value. $EISF_{\text{rot}}$ expresses the local constraint for the three-fold-rotational motion of the ion:

$$EISF_{\text{rot}} = \frac{1}{3}\left(1 + 2\frac{\sin\left(\sqrt{3}QR\right)}{\sqrt{3}QR}\right), \qquad (24)$$

with $R$ as the radius of the circle that is spanned with the motion. According to literature[44] $R$ is 2.6Å. Therefore it was fixed at this value. $f_{\text{r}}$ gives the fraction of hydrogen atoms, that are actually involved in the rotation. Since this process is not visible at high temperatures, the fit results depend here only on the low temperature data. But considering the rotational process improves the fit slightly also at high temperatures. We point out that the microscopic model we assume is compatible with data, but probably not the only one possible. Because the contribution of this process is small ($f_r = 0.038$), there is no significant influence of the choice of model to be expected on the parameters of the diffusional process.

Finally, the complete fitting function takes the following form:

$$I(Q,t) = A(T)\left(\left(1 - EISF_{\Phi}\right) I_{\text{rot}}(Q,t)\Phi(t) + EISF_{\Phi}\right) \qquad (25)$$

$A(T)$ describes the temperature-dependent amplitude, derived from the Debye-Waller-Factor

$$A = \exp\left[-BT - CT^2\right] \qquad (26)$$

and $EISF_{\Phi}$ is the EISF of the final relaxation as used in the Kohlrausch approach before. Because the inelastic neutron scattering methods used here do not allow a measurement of processes faster than 0.2 ps, their effect on $I(Q,t)$ has to be comprised in a Debye-Waller factor term. Such processes are likely to be harmonic vibrations, anharmonic effects and fast relaxations. However the expression has to be seen as an empirical postulate to fix this parameter in case it cannot be determined from the data. For harmonic vibrations one would expect a linear increase of the mean-square displacement with temperature motivating the term $-BT$ in the exponent. Because this term was not sufficient to describe the actual data, the term $-CT^2$ was added, possibly reflecting anharmonic effects and fast relaxations. Global fit parameters are then $\tau'$, $E$, $f_r$, $\tau_{\text{rot}}$, $B$ and $C$. In order to achieve the best fitting performance we first fitted temperature-dependent data at fixed $Q$ values. The values thus obtained were cross-checked with results from different $Q$ values, covering in total a range from 0.455 to 1.77$\text{Å}^{-1}$. Subsequently we fixed the global parameters and fitted the relaxation-times $\tau_{\text{avg}}$ for the same $Q$ range with fixed temperatures.

Fig. 8 shows data for $Q = 1.77$ $\text{Å}^{-1}$ in a temperature range from 200 to 430 K. Temperature dependences of $\tau_{\text{avg}}$ and $\sigma$ are discussed in the following section V A.

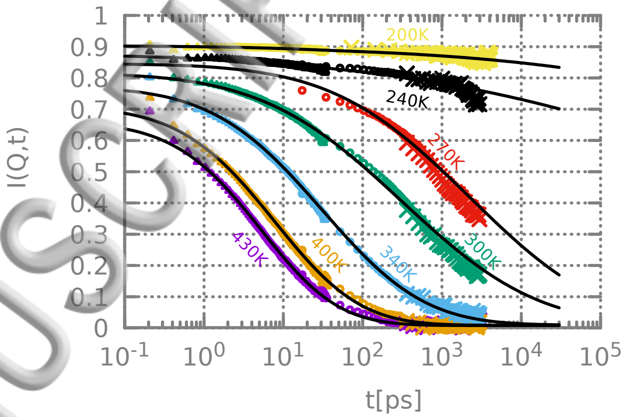

FIG. 8. Fit for QENS data at 1.77 $\text{Å}^{-1}$ in a temperature range from 200 K to 430 K with the distribution model. CNCS (△), BASIS (○) and SPHERES (×). Temperatures are indicated by the labels next to the data (different colors of the symbols online). For CNCS and BASIS the error bars are smaller than the symbol size for SPHERES roughly the size of the symbol.

TABLE III. Global fit parameters for fit with distribution model

| parameter | | value |
|---|---|---|
| $B$ | [$\text{Å}^2$/K] | $(1.20 \pm 0.09) \times 10^{-4}$ |
| $C$ | [$\text{Å}^2$/K] | $(2.04 \pm 0.04) \times 10^{-6}$ |
| $R$ | [Å] | 2.6 |
| $\tau'$ | [ps] | 0.03 |
| $E$ | [kJ/R] | $1.74 \pm 0.43$ |
| $f_r$ | | $0.038 \pm 0.001$ |

$Q$-dependent fits at 430 K, 400 K and 340 K are shown in Fig. 9, 10 and 11.

The physical interpretation of this kind of distribution model would imply individual diffusion processes of the form

$$I(Q,t) = \exp(-DQ^2 t) \qquad (27)$$

Thus for the individual processes $\tau = 1/Dt^2$ and for the average one expects

$$\tau_{\text{avg}} \propto Q^{-2}, \tag{28}$$

However, Fig. 12 shows that resulting $\tau$ values from Fig. 9, 10 and 11 are not following this simple diffusion behavior. The $Q$ dependence even does not follow a power law over the whole $Q$ range. Only for the range $0.445 - 1.376\text{Å}^{-1}$ a description is possible by

$$\tau_{\text{avg}} \propto Q^{-n}, \tag{29}$$

with an almost temperature-independent $n = 2.5$. The difference of the exponent from the expected value of 2 here (and also in the case of the Kohlrausch fit before) hints at a fundamentally different model based on diffusion on a fractal.

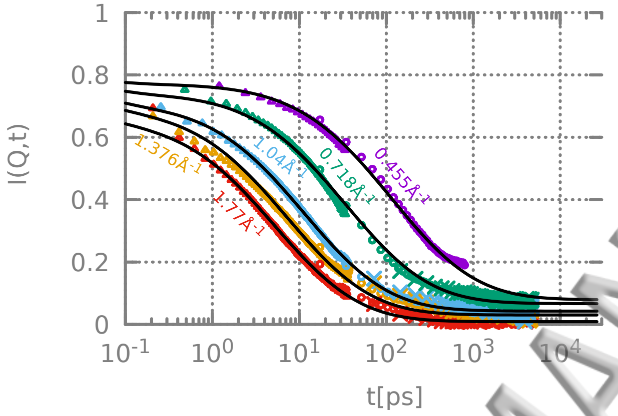

FIG. 9. Fit for QENS data at 430 K in a $Q$ range from 0.455 to 1.77 $\text{Å}^{-1}$ with the distribution model. CNCS (△), BASIS (○) and SPHERES (×). $Q$ values are indicated by the labels next to the data (different colors of the symbols online). For CNCS and BASIS the error bars are smaller than the symbol size for SPHERES roughly the size of the symbol.

Of course, equation 18 also covers the Kohlrausch function. A calculation of the implicit distribution function is possible by inverse Laplace transform[45,46]. Fig. 13 shows the probability density function of the log-Normal model in comparison with the implicit Kohlrausch distribution. The comparison shows that both distribution functions are fundamentally different. While the log-Normal distribution is symmetric on the logarithmic scale by definition, the distribution function belonging to the Kohlrausch function has a 'fat tail' on the left side. For the description of the data the log-Normal distribution performs slightly better. Therefore, we finally stayed with that choice.

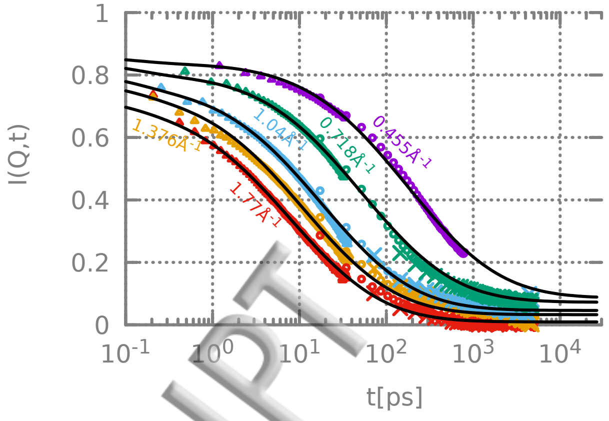

FIG. 10. Fit for QENS data at 400 K in a $Q$ range from 0.455 to 1.77 $\text{Å}^{-1}$ with the distribution model CNCS (△), BASIS (○) and SPHERES (×). $Q$ values are indicated by the labels next to the data (different colors of the symbols online). For CNCS and BASIS the error bars are smaller than the symbol size for SPHERES roughly the size of the symbol.

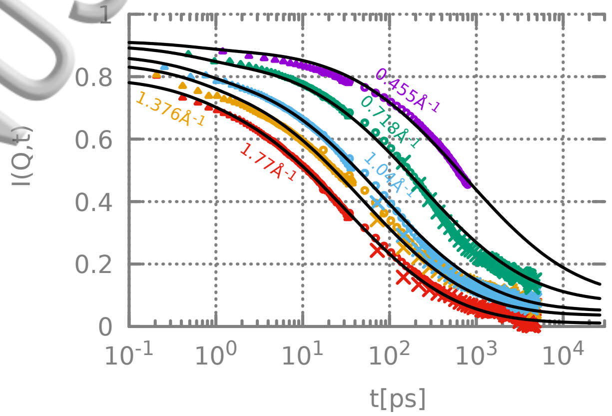

FIG. 11. Fit for QENS data at 340 K in a $Q$ range from 0.455 -to 1.77 $\text{Å}^{-1}$ with the distribution model. CNCS (△), BASIS (○) and SPHERES (×). $Q$ values are indicated by the labels next to the data (different colors of the symbols online). For CNCS and BASIS the error bars are smaller than the symbol size for SPHERES roughly the size of the symbol.

### C. Fractal Model

The need for a model with sub-diffusive behaviour means a need for a model with a somehow hindered diffusion. One model that fulfills that need and is motivated additionally by structural investigations[27,47], is that of diffusion on fractal structures. The latter is an often discussed topic (e.g.[48–50]) with quite a variety of approaches. We first want to illuminate the sub-diffusive nature of such a regime: The mean-square displacement for normal diffusion is given by:

$$\langle r^2 \rangle \propto t. \tag{30}$$

In the mean-square displacement the obstruction of the diffusive motion manifests itself as a subdiffusive regime:

$$\langle r^2 \rangle_{\text{frac}} \propto t^n, \text{with } n < 1. \tag{31}$$

In a normal regime, as described by equation (30), the

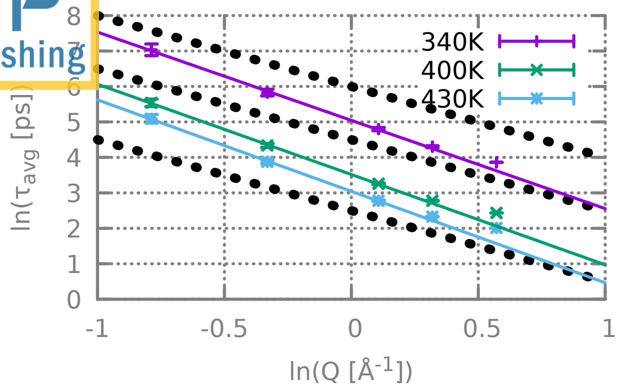

FIG. 12. $Q$ dependence of relaxation times $\tau$ for three different temperatures, dotted lines correspond to $n = 2$

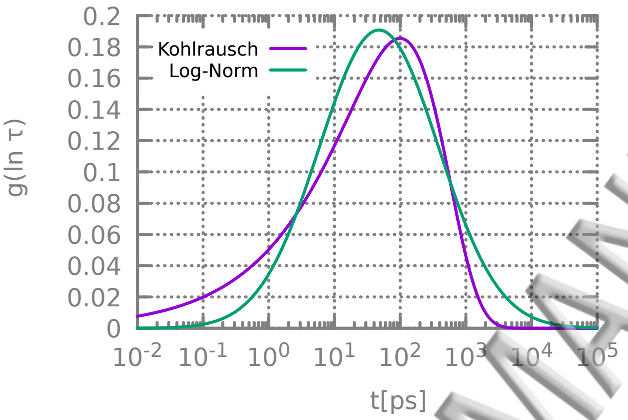

FIG. 13. Comparison of the relaxation time distribution of the Kohlrausch function and the log-Normal distribution at 340 K and 1.77Å$^{-1}$.

equation of motion is given by Fick's law:

$$\frac{\partial\rho}{\partial t} = \frac{1}{r^2}\frac{\partial}{\partial r}\left(Dr^2\frac{\partial\rho}{\partial r^2}\right). \qquad (32)$$

Following the approach of O'Shaughnessy and Procaccia[51], on a fractal $D$ is not constant anymore, but replaced by a diffusion $K(r)$ with spatial dependence:

$$K(r) = Kr^{-(d_w-2)} \qquad (33)$$

where $K$ is the fractal analog to the diffusion constant $D$.

Changing from diffusion on Euclidean lattices to diffusion on lattices of fractal dimension one needs to adjust the term $r^2$ resulting from the dimensionality in equation (32) as well[51]: The necessary amendment is to replace the exponent 2 by $d_f - 1$. Here, $d_f$ is the Hausdorff dimension of the fractal object. The equation of motion becomes then:

$$\frac{\partial\rho}{\partial t} = \frac{1}{r^{d_f-1}}\frac{\partial}{\partial r}\left(K(r)r^{d_f-1}\frac{\partial\rho}{\partial r}\right). \qquad (34)$$

For systems embedded in three-dimensional space $1 \leq d_f \leq 3$ and $d_w \geq 2$.

The solution for (34) is given as[51]:

$$\rho(r,t) = \frac{d_w}{d_f\Gamma(d_f/d_w)}\left(K{d_w}^2t\right)^{-d_f/d_w}\exp\left[-\frac{r^{d_w}}{K{d_w}^2t}\right]. \qquad (35)$$

The exact value of $\langle r^2\rangle$ is in this case given with[51]:

$$\langle r^2\rangle = \frac{\Gamma\left(\frac{(d_f+2)}{d_w}\right)}{\Gamma\left(\frac{d_f}{d_w}\right)}\left(Kd_w^2t\right)^{\frac{2}{d_w}}. \qquad (36)$$

Obviously subdiffusivity is given, since

$$\langle r^2\rangle \propto t^{\frac{2}{d_w}}, \qquad (37)$$

with $d_w > 2$ and $d_w$ turns out to be the exponent determining the power law, the random walk dimension.

To interpret equation (35) as van Hove correlation function (2) one has to note that in (35) $\rho$ is defined on the fractal structure, while $G(r,t)$ is defined on three-dimensional Euclidean space. Therefore, the two are related by

$$G(r,t) = \frac{d_f}{4\pi}r^{d_f-3}\rho(r,t). \qquad (38)$$

We can calculate the intermediate scattering function by Fourier transform:

$$S_{\text{frac}}(Q,t) = \Psi\cdot\int_0^\infty \exp\left[-\frac{x^{d_w}}{d_w^2\vartheta}\right]x^{d_f-2}\sin x dx. \qquad (39)$$

with

$$\Psi = \frac{d_w^{1-2d_f/d_w}}{\Gamma(d_f/d_w)\vartheta^{d_f/d_w}}. \qquad (40)$$

Equation (39) depends only on the rescaled time

$$\vartheta = Q^{d_w}Kt, \qquad (41)$$

implying that for any reasonably defined effective $\tau_{\text{eff}}$:

$$\tau_{\text{eff}}(Q) \propto Q^{-d_w}. \qquad (42)$$

Analogously to the distribution fit we introduced an amplitude $A(Q,T)$:

$$A(Q,T) = \exp\left[(-M - Q^2)(B'T + C'T^2)\right] \qquad (43)$$

Contrary to the previous model we fitted simultaneously temperature and $Q$ dependence. Hence the latter has to be considered when amending equation (26) to fit for the fractal model. The obvious adjustment would be then to introduce a $Q^2$ dependence in the exponent. It turned out that in this way it was not possible to fit the low $Q$ data. The reason for this is probably multiple scattering which can be included by an additional $Q$-independent term $M$. Finally, we used the same rotational function as introduced earlier for the distribution fit (compare (22)). The complete description is thus given by:

$$I(Q,t) = A(Q,T)I_{\mathrm{rot}}(Q,t)I_{\mathrm{frac}}(Q,t) \qquad (44)$$

We assumed $d_f$ to be temperature-independent, since we don't expect massive structural changes in the observed temperature range. Consequently $d_f$ is a global fit parameter. In the same way we managed to fit the scaling parameter $d_w$ globally as well. Comparing equation (29) and Fig.12 with (42), one expects $d_w$ to be comparable with $n$. Indeed we found $d_w = 2.46$.

Fig. 14–17 show the results for the fractal fit in the discussed $Q$ range of $0.455 - 1.113\text{Å}^{-1}$ and four different temperatures. The results were obtained by a simultaneous fit and are only shown in separated figures. The data for $Q = 1.77\,\text{Å}^{-1}$ have been omitted from the beginning because the respective points in figures 7 and 12 clearly do not fall on the power law line anymore. This shows that either the fractal structure breaks down at the corresponding length scale (about 3.5 Å) or we are seeing a transition to a hopping regime as found in glass-forming polymers[52]. It also turned out that the inclusion of $Q = 1.376\,\text{Å}^{-1}$ into the fit leads to instabilities. But in all cases except $T = 300$ K the theoretical curves calculated on the basis of $Q = 0.455$–$1.113\,\text{Å}^{-1}$ also fit that higher $Q$ value.

For temperatures $T \leq 270$ K the fractal model was inapplicable—at least with unchanged values of $d_f$ and $d_w$. This seems to indicate that there is a broadening of the relaxation as implied by the distribution model in addition to the broadening from fractality.

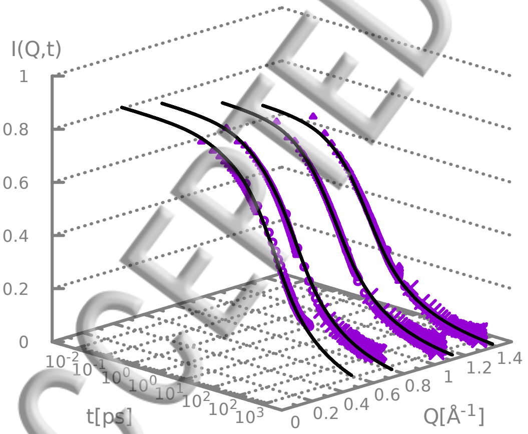

FIG. 14. Fit for QENS data at 430 K in a $Q$ range from 0.455 to 1.376 $\text{Å}^{-1}$ with the fractal model. CNCS (△), BASIS (○) and SPHERES (×).

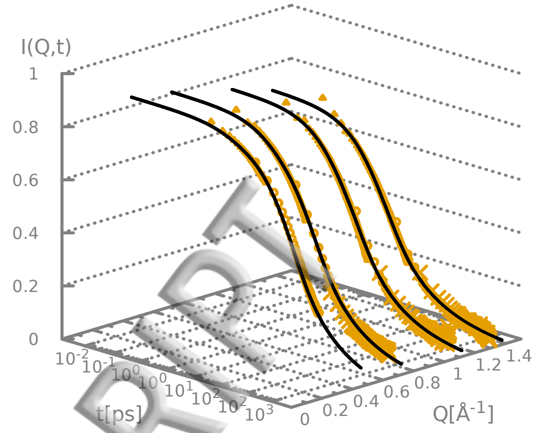

FIG. 15. Fit for QENS data at 400 K in a $Q$ range from 0.455 to 1.376 $\text{Å}^{-1}$ with the fractal model. CNCS (△), BASIS (○) and SPHERES (×).

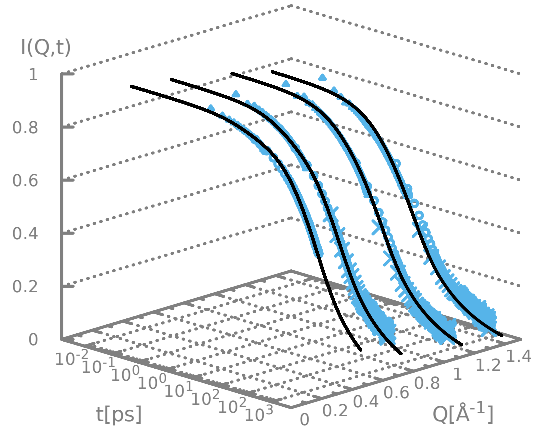

FIG. 16. Fit for QENS data at 340 K in a $Q$ range from 0.455 to 1.376 $\text{Å}^{-1}$ with the fractal model. CNCS (△), BASIS (○) and SPHERES (×).

## V. DISCUSSION

### A. Distribution model

In the heterogeneous picture of activated processes one expects that the distribution of relaxation times originates from a distribution of activation energies $E_A$. In

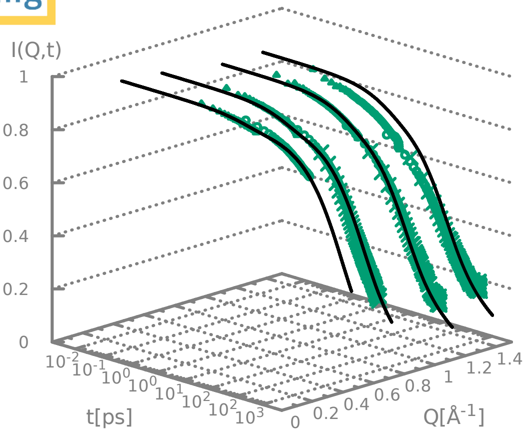

FIG. 17. Fit for QENS data at 300 K in a $Q$ range from 0.455 to 1.376 Å$^{-1}$ with the fractal model. CNCS (△), BASIS (○) and SPHERES (╳).

TABLE IV. Global fit parameters for fractal fit

| parameter | | value |
|---|---|---|
| $d_w$ | | $2.46 \pm 0.02$ |
| $d_f$ | | $1.09 \pm 0.08$ |
| $B'$ | [Å$^2$/K] | $(-0.44 \pm 0.04) \times 10^{-5}$ |
| $C'$ | [Å$^2$/K$^2$] | $(0.54 \pm 0.06) \times 10^{-6}$ |
| $M$ | [Å$^{-2}$] | $1.65 \pm 0.02$ |

the case of the log-Normal distribution for $g(\ln \tau)$ this would be a Normal distribution of $E_A$. The Arrhenius relation for the individual processes,

$$\tau = \tau_0 \exp\left[\frac{E_A}{k_B T}\right], \tag{45}$$

implies that the average relaxation time is

$$\tau_{\text{avg}} = \tau_0 \exp\left[\frac{\langle E_A \rangle}{k_B T}\right] \tag{46}$$

and $\sigma$ is then given by

$$\sigma = \frac{\Delta E_A}{k_B T} \tag{47}$$

However, the data in Fig.18 show a deviation from Arrhenius law. This is usually handled by introducing the empirical Vogel-Fulcher relation:

$$\tau_{\text{avg}} = \tau' \exp\left[\frac{B}{T - T_0}\right], \tag{48}$$

with the transition temperature $T_0$ and an energy parameter $B$. Here the assignment of the width of the distribution of relaxation times to distributions of the material parameters is not as clear as in the Arrhenius case. Assuming a distribution of the energy parameter $B$ would result in

$$\sigma = \frac{1}{T - T_0} \Delta B \tag{49}$$

Alternatively, a distribution of $T_0$ leads to

$$\sigma = \frac{B}{(T - T_0)^2} \Delta T_0. \tag{50}$$

Finally one can combine both assumptions leading to the expression:

$$\sigma = \sqrt{\left(\frac{\Delta B}{T - T_0}\right)^2 + \left(\frac{B \Delta T_0}{T - T_0}\right)^2}. \tag{51}$$

For our data an approach with distributed $T_0$ did not bring an improvement over equation (49). Therefore a distribution of the energy parameter $B$ only was assumed as the reason for the distribution of relaxation times. As Fig. 19 shows, in this way a good representation of $\sigma(T)$ is possible with the parameters of the Vogel-Fulcher law ($B, T_0$) and one additional parameter $\Delta B$.

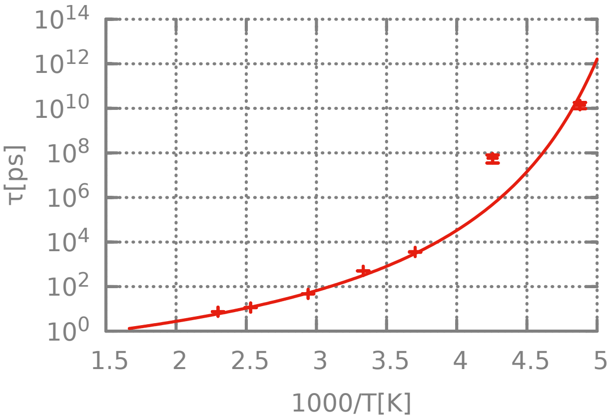

FIG. 18. Temperature dependence of average relaxation times times from Fig.8

TABLE V. parameters for the VFT Fit of $\tau_{\text{avg}}$ and $\sigma$ for Q= 1.77Å$^{-1}$ as defined in equation (49)

| | | Fit of $\tau_{\text{avg}}$(T) | Fit of $\sigma$(T) |
|---|---|---|---|
| $T_0$ | [K] | $158 \pm 4$ | $159 \pm 4$ |
| $B$ | [K] | $1158 \pm 102$ | – |
| $\Delta B$ | [K] | – | $392 \pm 12$ |
| $\tau_0$ | [ps] | $0.11 \pm 0.03$ | – |

Although there seem to be considerable systematic errors in the $\tau_{\text{avg}}$ and $\sigma$ values at low temperatures, the fits

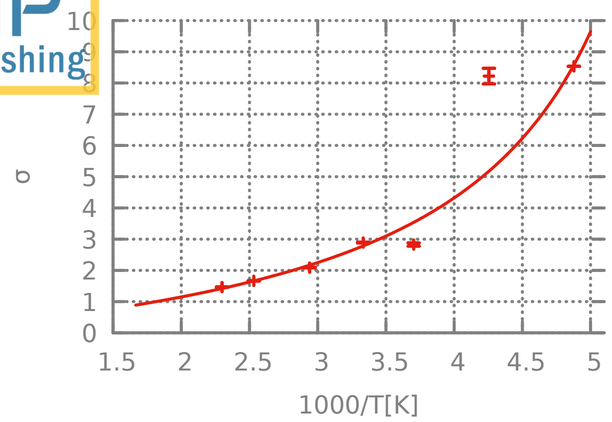

FIG. 19. Temperature dependence of width of distributions of relaxation times from Fig.8

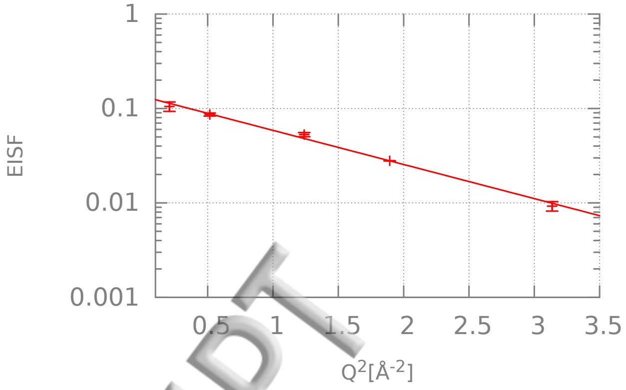

FIG. 20. Fit of $EISF_\Phi$ with equation (52)

demonstrate that a consistent description of both values using a Vogel-Fulcher law with distributed $B$ is possible. Tab. V shows the obtained fitting parameters. From the fit of $\tau(T)$ $\tau_0$, $B$ and $T_0$ were derived, from that of $\sigma$ $\Delta B$ and independently $T_0$.

We mentioned earlier, that we had to introduce an additional $EISF_\Phi$ to describe the data sufficiently for high temperatures and long times. The physical meaning is that a certain amount of protons is hindered in its motion and therefore fixed to a certain range of motion. In order to assign a length scale to the confinement we assume for the EISF:

$$EISF(Q) = \lim_{t\to\infty} I(Q,t) = P\exp\left[\frac{-Q^2\left\langle u^2\right\rangle}{3}\right]. \tag{52}$$

For small $Q$ values we expect:

$$\lim_{Q\to 0} P\exp\left[\frac{-Q^2\left\langle u^2\right\rangle}{3}\right] = P, \tag{53}$$

where $P$ is the fraction of particles confined to the length scale of $\langle u^2\rangle$. Intersection and slope of the fit in Fig.20 indicate that $\sim 13\%$ of the particles are confined to 0.16 nm at the longest time scale (5 ns).

It is important to notice that for the distribution model the time-temperature superposition (TTS) principle does not hold. For the fit with a Kohlrausch function (with fixed $\beta$) the data is described by a master function which is only rescaled by the relaxation time $\tau(Q,T)$. Therefore the width of the underlying distribution function is constant. Here, in contrast, $\sigma$ varies with temperature according to equation (51).

### B. Fractal model

In the Kohlrausch model for a homogeneous relaxation process a single parameter $\beta$ determines the stretching of $I(Q,t)$ as well as the $Q$ dependence of the time scale ( $\tau \propto Q^{-2/\beta}$ ). In the framework of the fractal model there are two parameters $d_f$ and $d_w$. While the $Q$ dependence is determined by $d_w$ only ( $\tau \propto Q^{-d_w}$ ), both $d_w$ and $d_f$ influence the stretching in time. In that way, both features of the data can be fitted without contradiction. (But it has to be conceded that this is only possible with an unusually low value of $d_f$.)

Fig. 21 shows that the temperature dependence of the earlier introduced fractal diffusion coefficient $K$ is following a similar trend as the Vogel-Fulcher behavior of $\tau_{\text{avg}}$ from the distribution model. However in the high temperature range we find an activation energy of 34 ± 6.5 kJ mol$^{-1}$, which is in very good agreement with findings of activation energies of diffusion coefficients, obtained by PFG-NMR[53]. Reported activation energies of conductivity have similar values as well[54], 32 . . . 34 kJ mol$^{-1}$ for 420 wt% doping. Values from QENS[34] and NMR[33] on phosphoric-acid-benzimidazole systems are systematically lower ($E_A = 20\ldots28$ kJ mol$^{-1}$), but one has to consider that these were unpolymerized systems. A comparison with our previous findings[27] shows a disagreement of the activation energy. That is probably due to the fact that those results were obtained using a different sample treatment and may have had a different ion concentration than the samples presented in this publication.

TABLE VI. parameters for VFT-Fit of $\tau_{\text{avg}}$ and $K$, corresponding plot is to be found in Fig. 21.

| | | Fit of $\tau_{\text{avg}}^{-1}$(T) | Fit of $K$(T) |
|---|---|---|---|
| $T_0$ | [K] | $158 \pm 6$ | $162 \pm 3$ |
| $B$ | [K] | $1158 \pm 102$ | $1082 \pm 31$ |
| $E_a$ | [kJ/mol] | – | $34 \pm 7$ |

For the fractal model with temperature independent factors $d_w$ and $d_f$ the TTS priciple is valid again. However the fractal model was only applied in a temper-

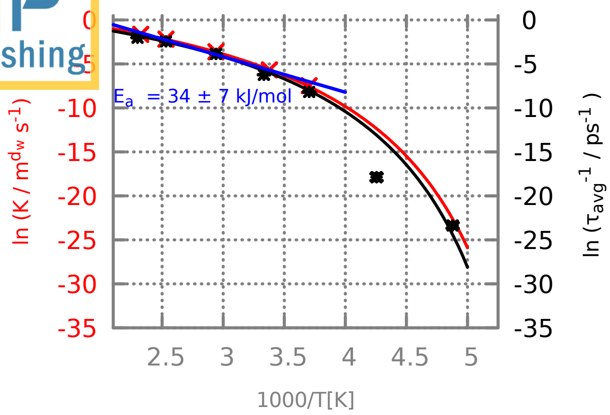

FIG. 21. Diffusion coefficients from the fractal model (red, left axis) and average relaxation frequencies (black, right axis) from the distribution model. The Vogel-Fulcher fits (lines with same colors) show that extrapolated down to 200 K both parameters have the same temperature dependence. The blue line shows the apparent Arrhenius law at high temperatures.

ature range above 270 K, therefore a deviation from TTS may be unnoticed. In this temperature range, as Fig. 19 shows, a rather constant broadening of distribution times. Indeed, the failure of the fractal model for lower temperatures indicates an additional temperature-dependent broadening (as in the distribution model).

Although the found fractal parameters $d_w$ and $d_f$ seem unusual, there are conceivable fractal system representing such values. Those systems however are very close to the linear case $d_f = 1$. More details are to be found in the supplementary materials. Note that the fits using the fractal model were done without an additional EISF (as for the distribution model). Fits with that addition did not provide a significant improvement. It seems that the very slow ($> 5$ ns) component of the dynamics is completely included in the algebraic tail of the fractal fit function. The alternative description by a distribution leads to a sharper cut-off and has to be complemented by a component interpretable as permanent confinement. A similar ambiguity in the interpretation was observed for a confined glass-forming liquid[55].

## VI. CONCLUSIONS

In this paper we present QENS results of $H_3PO_4$-doped PBI membranes. To obtain a purely incoherent signal from protons only we measured samples with approximately same amounts of $H_3PO_4$ and $D_3PO_4$ with the intention to dispose of contributions from the polymer chain by a subsequent subtraction of the two sample types. By using material-dependent macroscopic scattering cross sections of the samples we could get to a correct subtraction although we could not produce samples of exactly identical amounts of acid. To cover a time range from 0.1 ps to about 5 ns we combined Fourier-transformed data from Time-of-Flight, Backscattering and Time-of-Flight Backscattering instruments. For the data analysis we first used an empirical Kohlrausch law. A Kohlrausch function can be explained with two physical pictures: Assuming all particles relax identically with an intrinsically non-exponential behaviour one speaks of a homogeneous picture. The heterogeneous case then explains the stretched exponential decay by a distribution, caused by dynamic heterogeneities, of relaxation processes of the same type. The homogeneous picture turned out to be false because of inconsistent Kohlrausch exponent and $Q$ dependence of the relaxation time. For the second approach we used an explicitly formulated log-Normal distribution of simple relaxation processes. (The implicit Kohlrausch distribution function lacked the necessary flexibility to describe the heterogeneous case sufficiently.) However the second model was also inconsistent since the observed $Q$ dependence did not follow the expected $Q^{-2}$ diffusional behavior. The need for a subdiffusional description in an intermediate $Q$ range finally motivated the use of a fractal diffusion model, based on a description by O'Shaughnessy and Procaccia[51].

The obtained fractal dimensions help gaining a more concrete picture of the actual microscopic diffusion processes: The unusually small Hausdorff dimension $d_f = 1.09$ indicates close-to-linear diffusion pathways. The 'walk' dimension $d_w = 2.46$ shows a moderate deviation from ordinary diffusion ($d_w = 2$). We note that similar values of the exponents can be obtained from a modified Koch curve without claiming that the actual diffusion path has this shape. The deviation of $\tau(Q)$ from what is expected in the fractal model starting between 1.113 and 1.376 $\text{Å}^{-1}$ indicates that the lower border of the fractal regime is at about 5 Å. In order to determine the upper border further experiments utilizing pulsed field gradient NMR are planned.

Qualitatively, the results agree with the finding of subdiffusivity by Berrod et al.[21] in perfluoro-sulfonic acid (PFSA)/water systems. Although values of $d_w$ are not reported in this article, from figure 4 of that publication one can estimate $d_w = 2 \ldots 5$ with the higher values at high hydration levels comparable to those used here. The samples in ref. 21 and in our study differ strongly in their chemistry and structure. But since our investigation focuses on a rather local molecular scale ($2\pi/Q < 2$ nm) we attribute the difference in the fractal exponent to the class of materials (PFSA/water vs PBI/phosphoric acid) rather than particular modifications as the crosslinking.

## VII. SUPPLEMENTARY MATERIALS

**Theory of Models:** (pdf) A theoretical description of the log-Normal model and a modified Koch curve, i.e. one with an arbitrary value of $d_f$. Further the description of yet another approach to describe subdiffusivity, based on[56].

## VII. ACKNOWLEDGEMENTS

Neutron scattering experiments performed at ORNL's Spallation Neutron Source are supported by the Scientific User Facilities Division, Office of Basic Energy Sciences (BES), U.S. Department of Energy (DOE), under Contract No. DE-AC0500OR22725 with UT Battelle, LLC.

[1] J.-H. Wee, Renew. Sust. Energ. Rev. **11**, 1720 (2007).

[2] L. Zhang, S.-R. Chae, Z. Hendren, J.-S. Park, and M. R. Wiesner, Chem. Eng. J. **204–206**, 87 (2012).

[3] Q. Li, D. Aili, H. A. Hjuler, and J. O. Jensen, *High Temperature Polymer Electrolyte Membrane Fuel Cells – Approaches, Status, and Perspectives* (Springer, Cham, 2016).

[4] H. Vogel and C. S. Marvel, Journal of Polymer Science **50**, 511 (1961).

[5] J. S. Wainright, J.-T. Wang, D. Weng, R. F. Savinell, and M. Litt, Journal of The Electrochemical Society **142**, L121 (1995).

[6] R. F. Savinell and M. H. Litt, "Proton conducting polymers used as membranes, US Patent US005525436," (1996).

[7] J. Yang, R. He, and D. Aili, in *High Temperature Polymer Electrolyte Fuel Cells*, edited by Q. Li, D. Aili, H. A. Hjuler, and J. O. Jensen (Springer, Cham, 2016) Chap. 7, pp. 151–167.

[8] F. Volino and a.J. Dianoux, Molecular Physics **41**, 271 (1980).

[9] T. D. Gierke, G. E. Munn, and F. C. Wilson, Journal of Polymer Science: Polymer Physics Edition **19**, 1687 (1981).

[10] L. Rubatat, A. L. Rollet, G. Gebel, and O. Diat, Macromolecules **35**, 4050 (2002).

[11] L. Rubatat, G. Gebel, and O. Diat, Macromolecules **37**, 7772 (2004).

[12] A. M. Pivovar and B. S. Pivovar, The journal of physical chemistry. B **109**, 785 (2005).

[13] M. H. Kim, C. J. Glinka, S. A. Grot, and W. G. Grot, Macromolecules **39**, 4775 (2006).

[14] F. Volino, J. C. Perrin, and S. Lyonnard, Journal of Physical Chemistry B **110**, 11217 (2006).

[15] J.-C. Perrin, S. Lyonnard, and F. Volino, Journal of Physical Chemistry C **111**, 3393 (2007).

[16] J. C. Perrin, S. Lyonnard, F. Volino, and A. Guillermo, European Physical Journal: Special Topics **141**, 57 (2007).

[17] K. Schmidt-Rohr and Q. Chen, Nature materials **7**, 75 (2008).

[18] R. Hempelmann, in *Solid State Proton Conductors: Properties and Applications in Fuel Cells*, edited by P. Knauth and M. L. di Vona (John Wiley & Sons, 2012) 1st ed., Chap. 4, pp. 71–108.

[19] F. Volino, M. Pineri, A. J. Dianoux, and A. De Geyer, J. Polym. Sci.: Polym. Phys. Ed. **20**, 481 (1982).

[20] P. L. Hall and D. K. Ross, Molecular Physics **42**, 637 (1981).

[21] Q. Berrod, S. Hanot, A. Guillermo, S. Mossa, and S. Lyonnard, Sci. Rep. **7**, 8326 (2017).

[22] Q. Li, J. O. Jensen, R. F. Savinell, and N. J. Bjerrum, Progress in Polymer Science **34**, 449 (2009).

[23] C. Wannek, W. Lehnert, and J. Mergel, Journal of Power Sources **192**, 258 (2009).

[24] P. Boillat, J. Biesdorf, P. Oberholzer, A. Kaestner, and T. J. Schmidt, Journal of the Electrochemical Society **161**, F192 (2013).

[25] T. Arlt, W. Lüke, N. Kardjilov, J. Banhart, W. Lehnert, and I. Manke, Journal of Power Sources **299**, 125 (2015).

[26] O. Holderer, O. Ivanova, B. Hopfenmüller, M. Zamponi, W. Maier, A. Majerus, W. Lehnert, M. Monkenbusch, and R. Zorn, International Journal of Hydrogen Energy **39**, 21657 (2014).

[27] O. Holderer, O. Ivanova, M. Khaneft, B. Hopfenmüller, W. Lüke, A. Majerus, M.-S. Appavou, N. Szekely, M. Krutyeva, E. Kentzinger, R. Zorn, and W. Lehnert, ECS Transactions **69**, 337 (2015).

[28] K.-D. Kreuer, A. Rabenau, and W. Weppner, Angew. Chem. **94**, 224 (1982).

[29] K.-D. Kreuer, S. J. Paddison, E. Spohr, and M. Schuster, Chem. Rev. **104**, 4637 (2004).

[30] R. Bouchet, S. Miller, M. Duclot, and J. Souquet, Solid State Ionics **145**, 69 (2001).

[31] J. R. P. Jayakody, S. H. Chung, L. Durantino, H. Zhang, L. Xiao, B. C. Benicewicz, and S. G. Greenbaum, Journal of The Electrochemical Society **154**, B242 (2007).

[32] J.-P. Melchior, G. Majer, and K.-D. Kreuer, Phys. Chem. Chem. Phys. **19**, 587 (2017).

[33] J.-P. Melchior, G. Majer, and K.-D. Kreuer, Phys. Chem. Chem. Phys. **19**, 601 (2017).

[34] J.-P. Melchior and B. Frick, Phys. Chem. Chem. Phys. **19**, 28540 (2017).

[35] F. Rieutord, "INX- Program for TOF data reduction https://www.ill.eu/instruments-support/computing-for-science/cs-software/all-software/tofhr/inx/ ," (1990).

[36] W. Schweika and P. Böni, Physica B: Condensed Matter **297**, 155 (2001).

[37] G. Ehlers, A. A. Podlesnyak, and A. I. Kolesnikov, Review of Scientific Instruments **87**, 093902 (2016), http://dx.doi.org/10.1063/1.4962024.

[38] J. Wuttke, A. Budwig, M. Drochner, H. Kämmerling, F.-J. Kayser, H. Kleines, V. Ossovyi, L. C. Pardo, M. Prager, D. Richter, G. J. Schneider, H. Schneider, and S. Staringer, The Review of scientific instruments **83**, 75109 (2012).

[39] Heinz Maier-Leibnitz Zentrum, Journal of large-scale facilities , A30 (2015).

[40] E. Mamontov and K. W. Herwig, The Review of scientific instruments **82**, 85109 (2011).

[41] The exact chemical composition of the benzimidazol copolymer is a trade secret. Therefore, the structure shown in figure 1(B) can only be seen as approximative.

[42] C. Korte, F. Conti, J. Wackerl, P. Dams, A. Majerus, and W. Lehnert, J. Appl. Electrochem. **45**, 857 (2015).

[43] R. Kohlrausch, Annalen der Physik und Chemie **91**, 179 (1854), reprinted in arXiv:9811186 [arXiv:cond-mat].

[44] R. Xia, Acta Crystallographica Section E: Structure Reports Online **65**, 115 (2009).

[45] F. Alvarez, A. Alegra, and J. Colmenero, Physical review. B, Condensed matter **44**, 7306 (1991).

[46] M. N. Berberan-Santos, Journal of Mathematical Chemistry **38**, 165 (2005).

[47] O. Ivanova, W. Lüke, A. Majerus, M. Krutyeva, N. K. Szekely, W. Pyckhout-Hintzen, M.-S. Appavou, M. Monkenbusch, R. Zorn, W. Lehnert, and O. Holderer, J. Membr. Sci. **533**, 342 (2017).

[48] S. Havlin, D. Movshovitz, B. Trus, and G. H. Weiss, Journal of Physics A: Mathematical and General **18**, L719 (1999).

[49] R. Guyer, Physical Review A **29**, 3 (1984).

[50] J. R. Banavar and J. F. Willemsen, Physical Review B **30**, 6778 (1984).

[51] B. O'Shaughnessy and I. Procaccia, Physical Review Letters **54**, 455 (1985).

[52] A. Arbe, J. Colmenero, F. Alvarez, M. Monkenbusch, D. Richter, B. Farago, and B. Frick, Phys. Rev. E **67**, 051802 (2003).

[53] M. Krutyeva, "Private communication," (2016).

[54] Y.-L. Ma, J. S. Wainright, M. H. Litt, and R. F. Savinell, Journal of The Electrochemical Society **151**, A8 (2004).

[55] R. Zorn, B. Frick, D. Richter, and F. Kremer, Journal of Non-Crystalline Solids **307-310**, 547–554 (2002).

[56] R. Metzler, W. G. Glöckle, and T. F. Nonnenmacher, Physica A: Statistical Mechanics and its Applications **211**, 13 (1994).

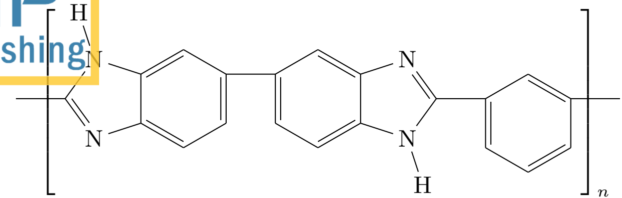

(A)

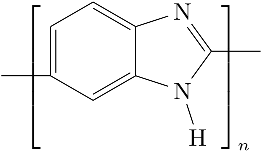

(B)

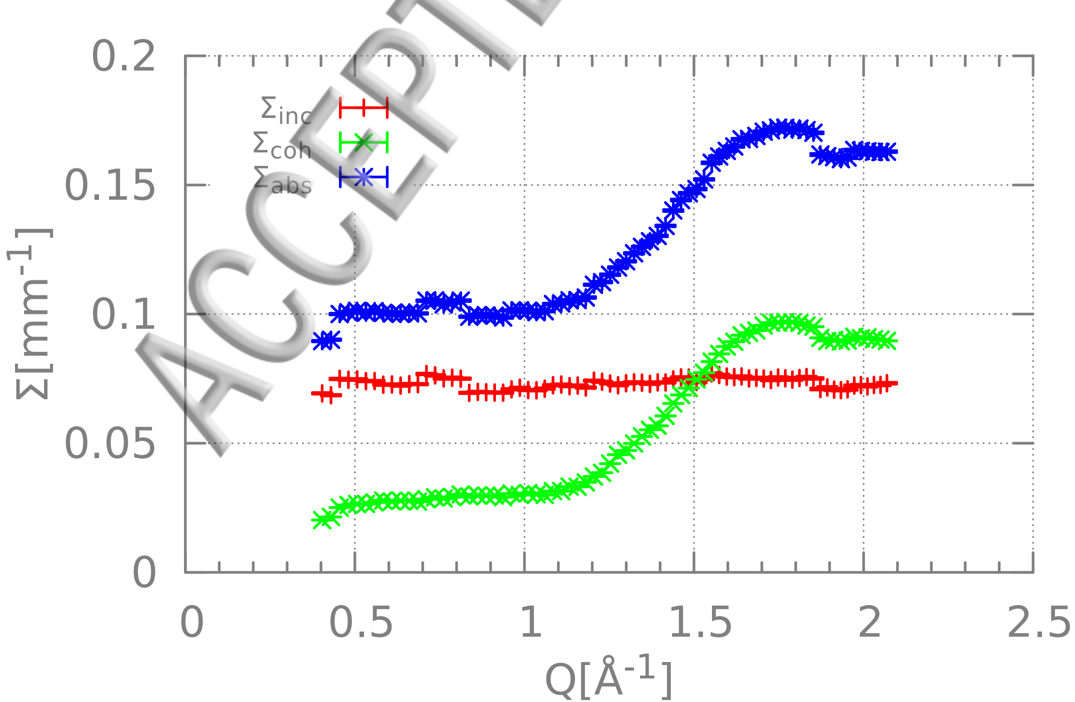
0.2
0.15
0.1
0.05
0
0
0.5
1
1.5
2
2.5
Σ[mm⁻¹]
Q[Å⁻¹]
Σinc
Σcoh
Σabs

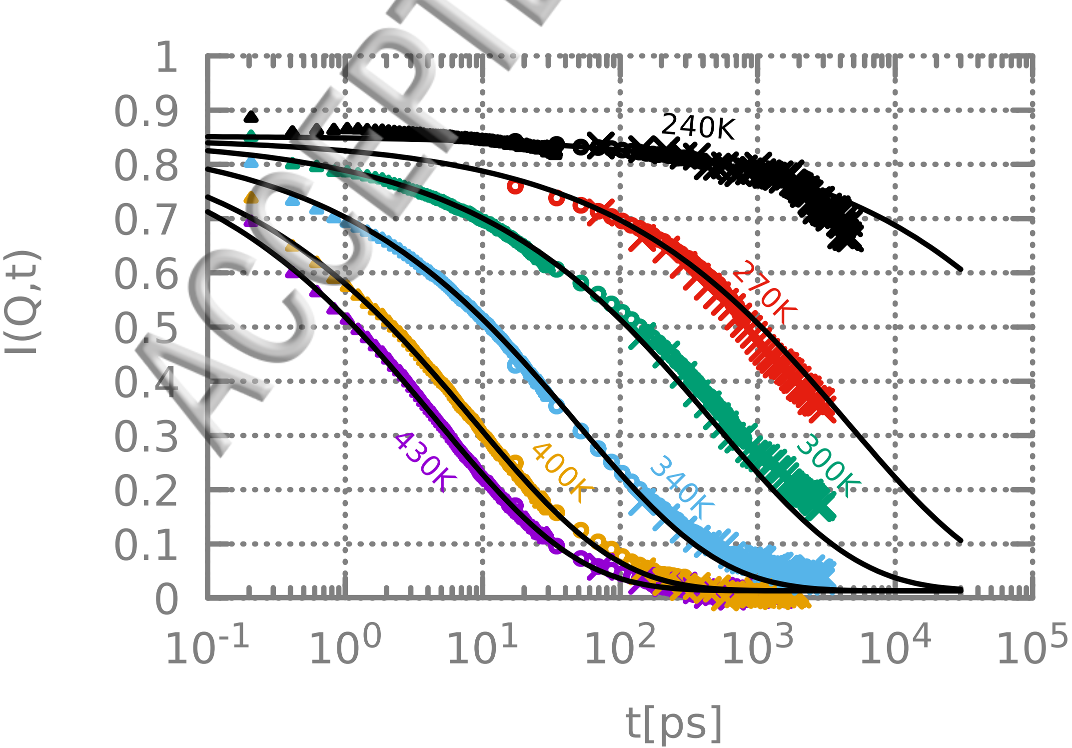

I(Q,t)
1
0.9
0.8
0.7
0.6
0.5
0.4
0.3
0.2
0.1
0
$10^{-1}$
$10^{0}$
$10^{1}$
$10^{2}$
$10^{3}$
$10^{4}$
$10^{5}$
t[ps]
240K
270K
300K
340K
400K
430K

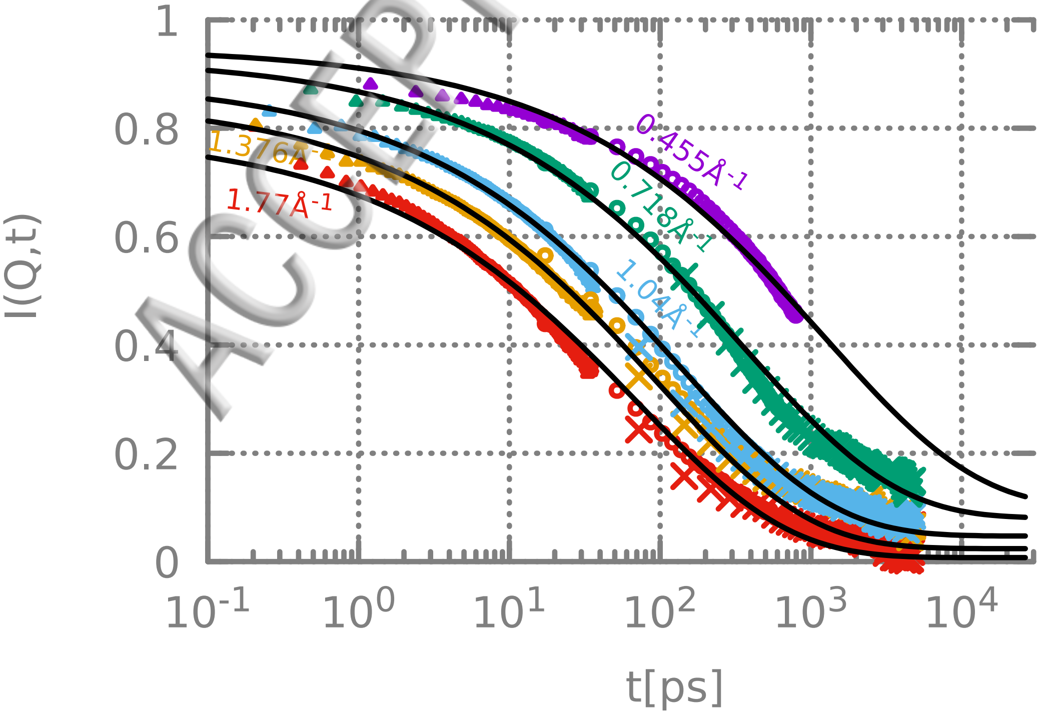
1
0.8
0.6
0.4
0.2
0
I(Q,t)
$10^{-1}$
$10^{0}$
$10^{1}$
$10^{2}$
$10^{3}$
$10^{4}$
t[ps]
0.455Å$^{-1}$
0.718Å$^{-1}$
1.04Å$^{-1}$
1.376Å$^{-1}$
1.77Å$^{-1}$

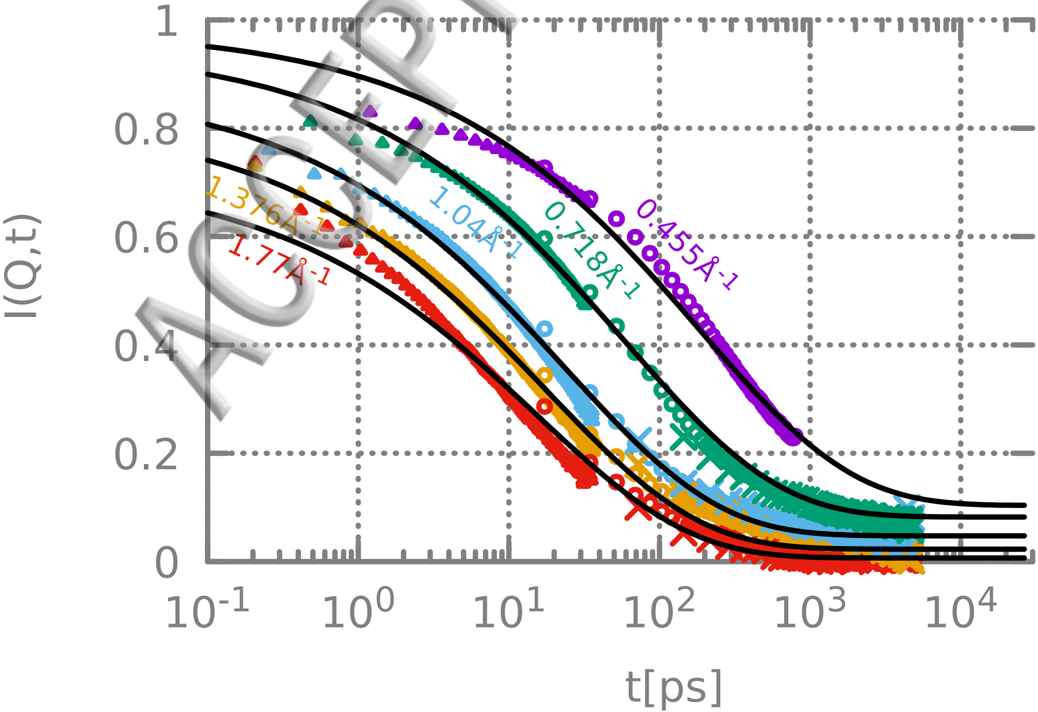
1
0.8
0.6
0.4
0.2
0
I(Q,t)
$10^{-1}$
$10^{0}$
$10^{1}$
$10^{2}$
$10^{3}$
$10^{4}$
t[ps]
0.455Å-1
0.718Å-1
1.04Å-1
1.376Å-1
1.77Å-1

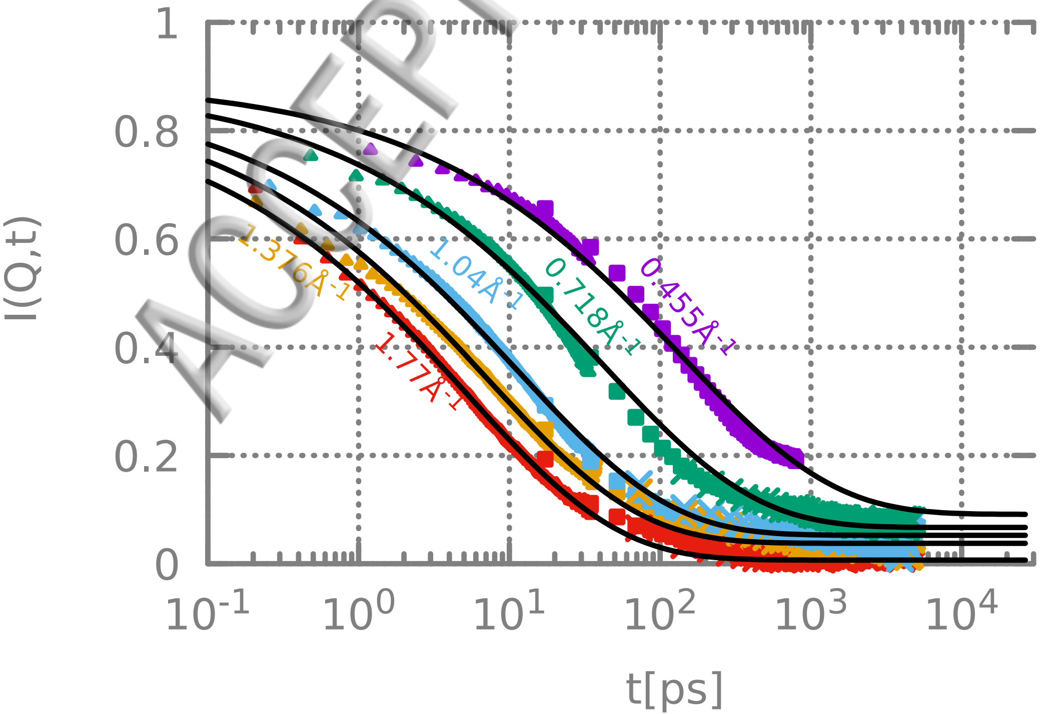
1
0.8
0.6
0.4
0.2
0
I(Q,t)
$10^{-1}$
$10^{0}$
$10^{1}$
$10^{2}$
$10^{3}$
$10^{4}$
t[ps]
1.376Å-1
1.04Å-1
0.718Å-1
0.455Å-1
1.77Å-1

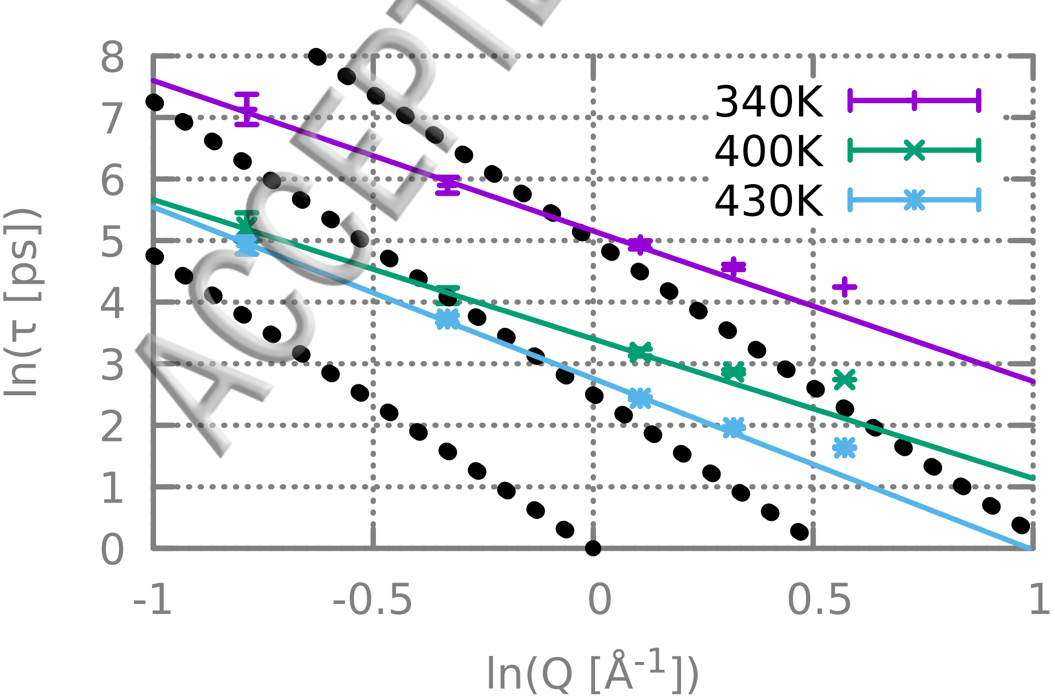

340K
400K
430K
ln(τ [ps])
ln(Q [Å$^{-1}$])
8
7
6
5
4
3
2
1
0
-1
-0.5
0
0.5
1

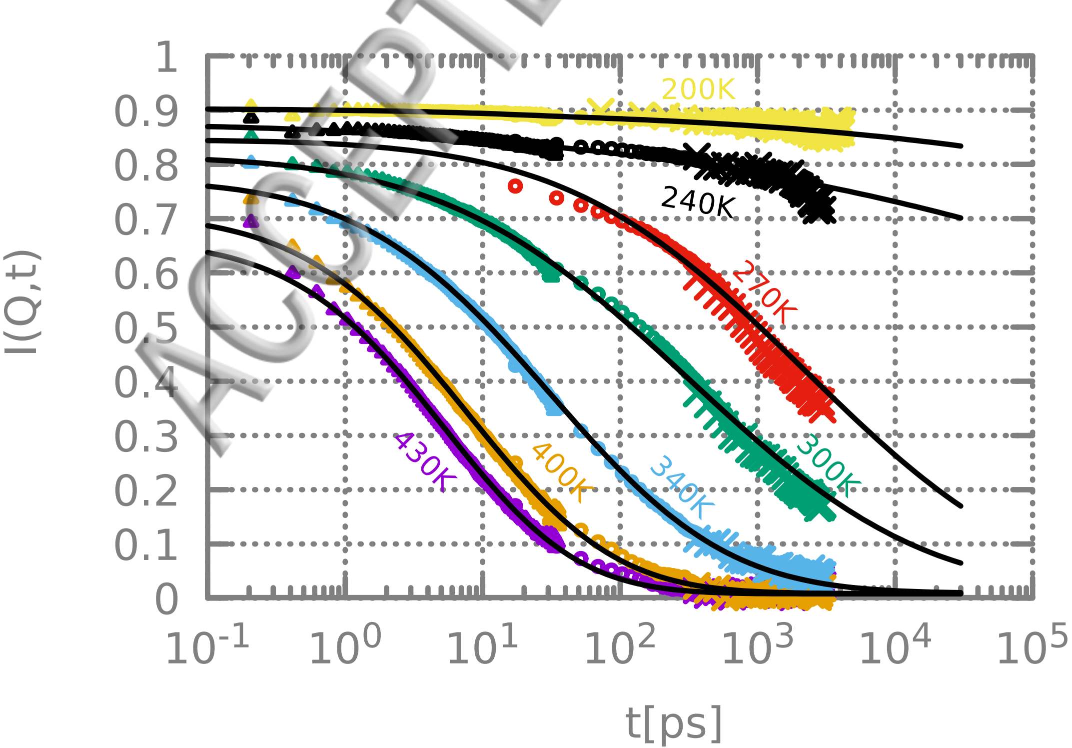
1
0.9
0.8
0.7
0.6
0.5
0.4
0.3
0.2
0.1
0
I(Q,t)
$10^{-1}$
$10^{0}$
$10^{1}$
$10^{2}$
$10^{3}$
$10^{4}$
$10^{5}$
t[ps]
200K
240K
270K
300K
340K
400K
430K

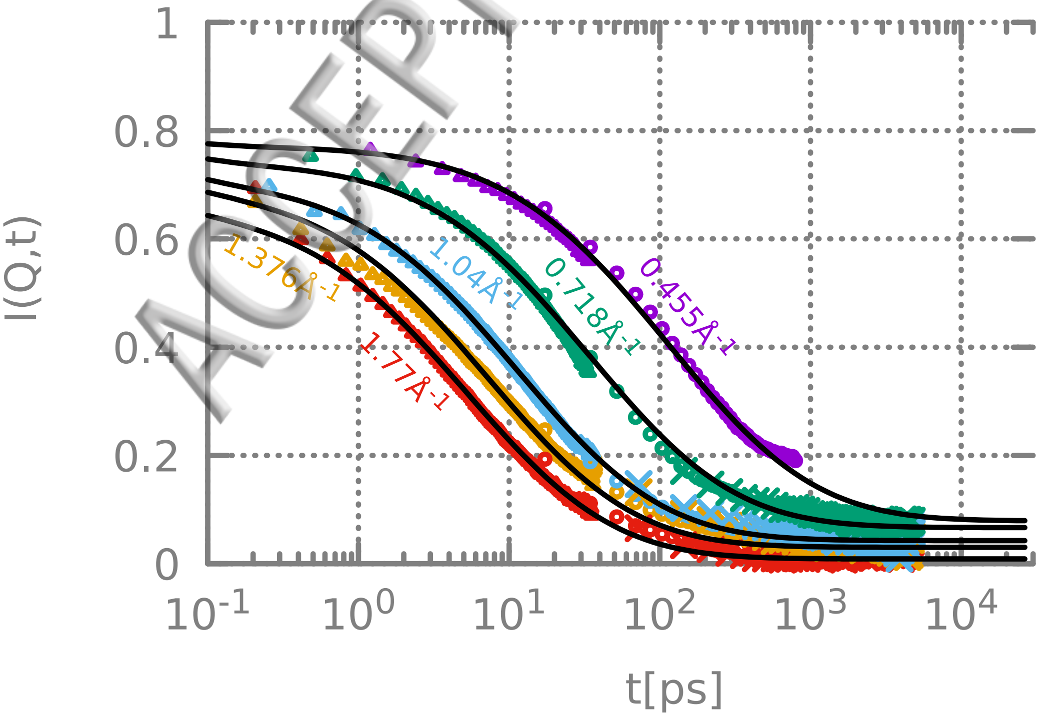
1
0.8
0.6
0.4
0.2
0
I(Q,t)
$10^{-1}$
$10^{0}$
$10^{1}$
$10^{2}$
$10^{3}$
$10^{4}$
t[ps]
1.376Å-1
1.04Å-1
0.718Å-1
0.455Å-1
1.777Å-1

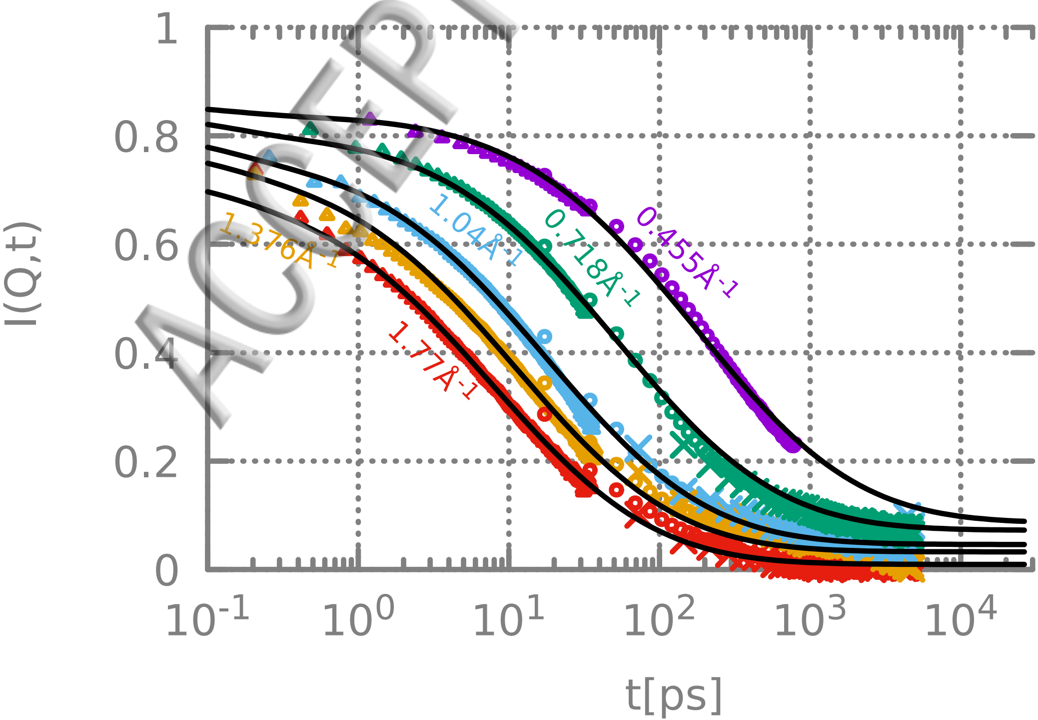
1
0.8
0.6
0.4
0.2
0
I(Q,t)
10^-1
10^0
10^1
10^2
10^3
10^4
t[ps]
0.455Å-1
0.718Å-1
1.04Å-1
1.376Å-1
1.77Å-1

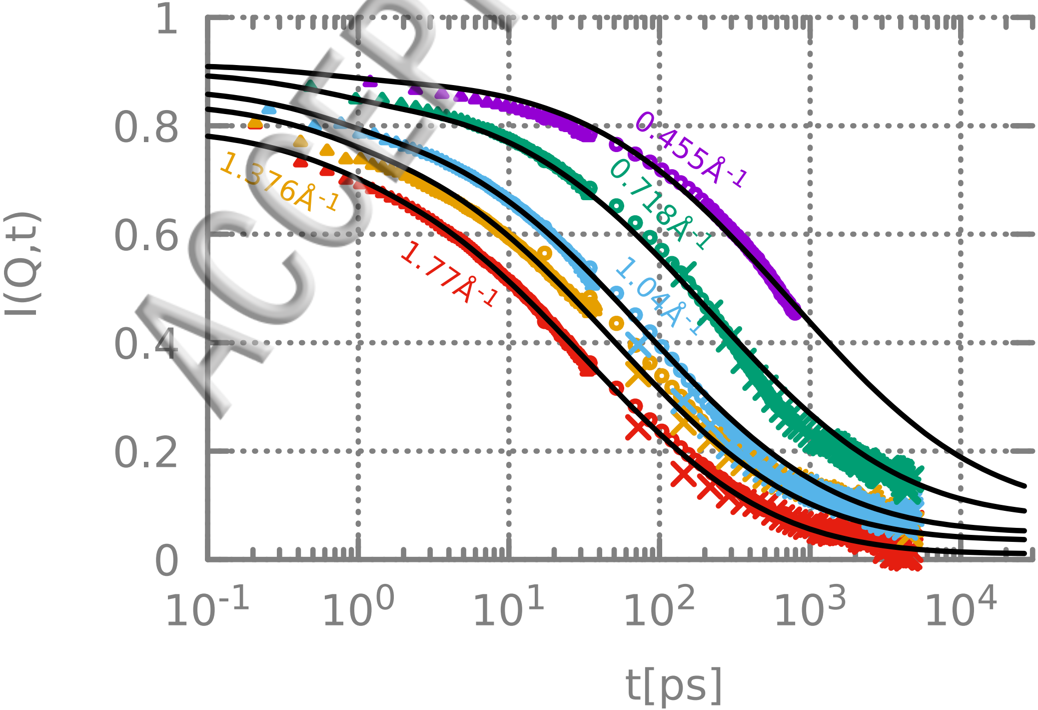
1
0.8
0.6
0.4
0.2
0
I(Q,t)
$10^{-1}$
$10^{0}$
$10^{1}$
$10^{2}$
$10^{3}$
$10^{4}$
t[ps]
0.455Å-1
0.718Å-1
1.04Å-1
1.376Å-1
1.77Å-1

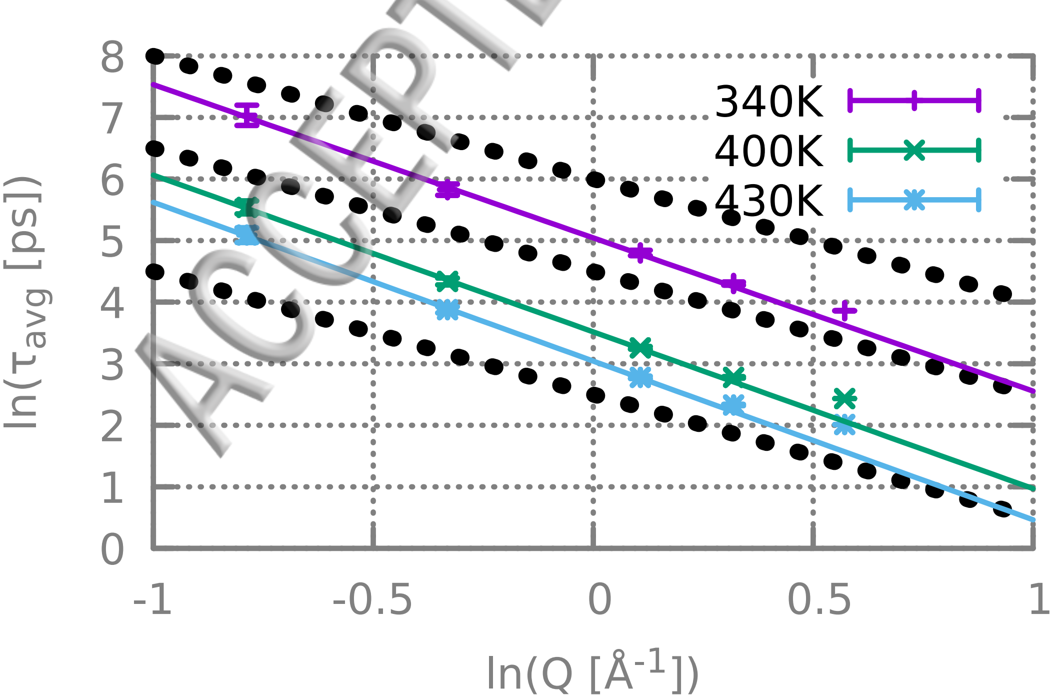

8
7
6
5
4
3
2
1
0
-1
-0.5
0
0.5
1
ln(τ_avg [ps])
ln(Q [Å^-1])
340K
400K
430K

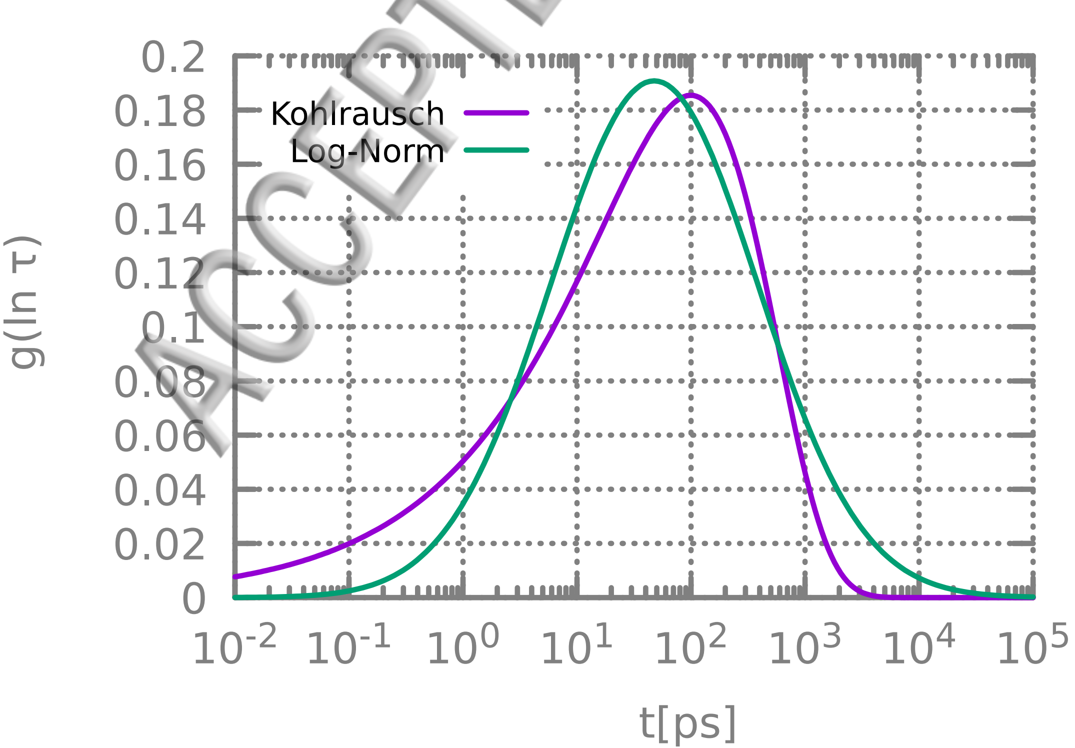
0.2
0.18
0.16
0.14
0.12
0.1
0.08
0.06
0.04
0.02
0
g(ln τ)
Kohlrausch
Log-Norm
$10^{-2}$
$10^{-1}$
$10^{0}$
$10^{1}$
$10^{2}$
$10^{3}$
$10^{4}$
$10^{5}$
t[ps]

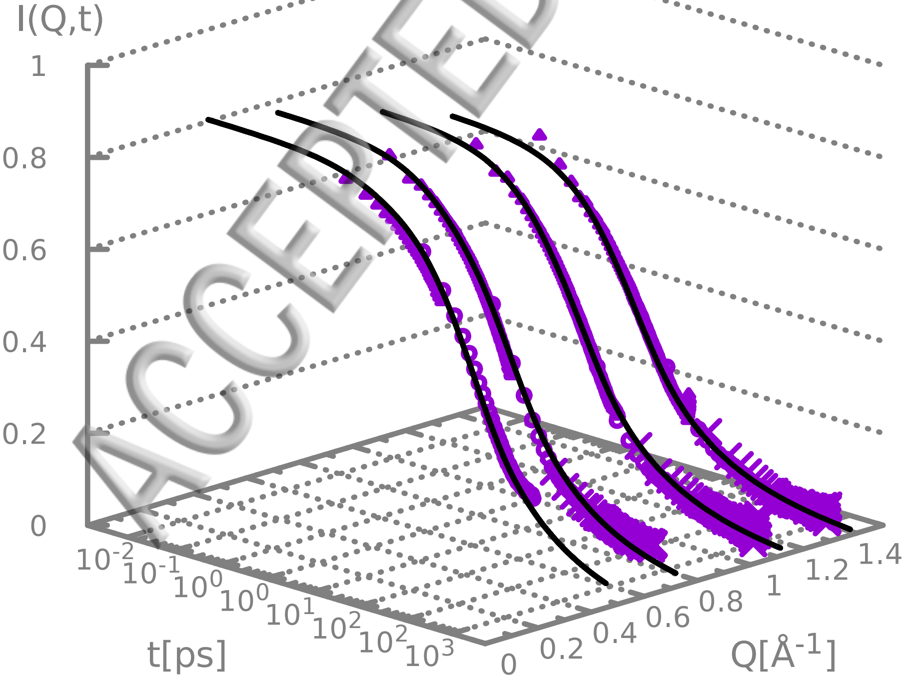
I(Q,t)
1
0.8
0.6
0.4
0.2
0
$10^{-2}$
$10^{-1}$
$10^{0}$
$10^{0}$
$10^{1}$
$10^{2}$
$10^{2}$
$10^{3}$
t[ps]
0
0.2
0.4
0.6
0.8
1
1.2
1.4
Q[Å$^{-1}$]

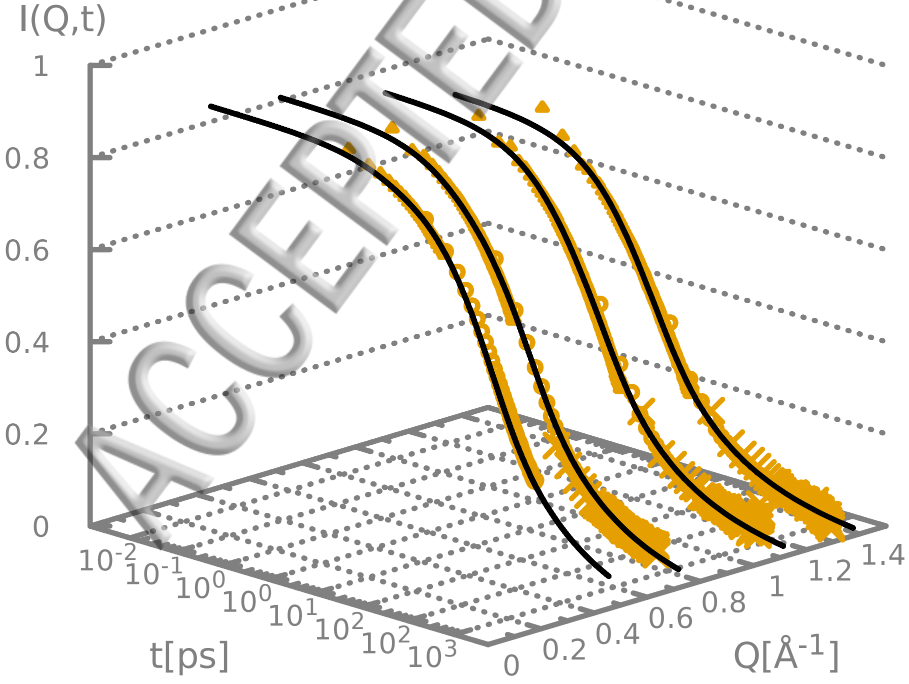
I(Q,t)
1
0.8
0.6
0.4
0.2
0
$10^{-2}$
$10^{-1}$
$10^{0}$
$10^{0}$
$10^{1}$
$10^{2}$
$10^{2}$
$10^{3}$
t[ps]
0
0.2
0.4
0.6
0.8
1
1.2
1.4
Q[Å$^{-1}$]

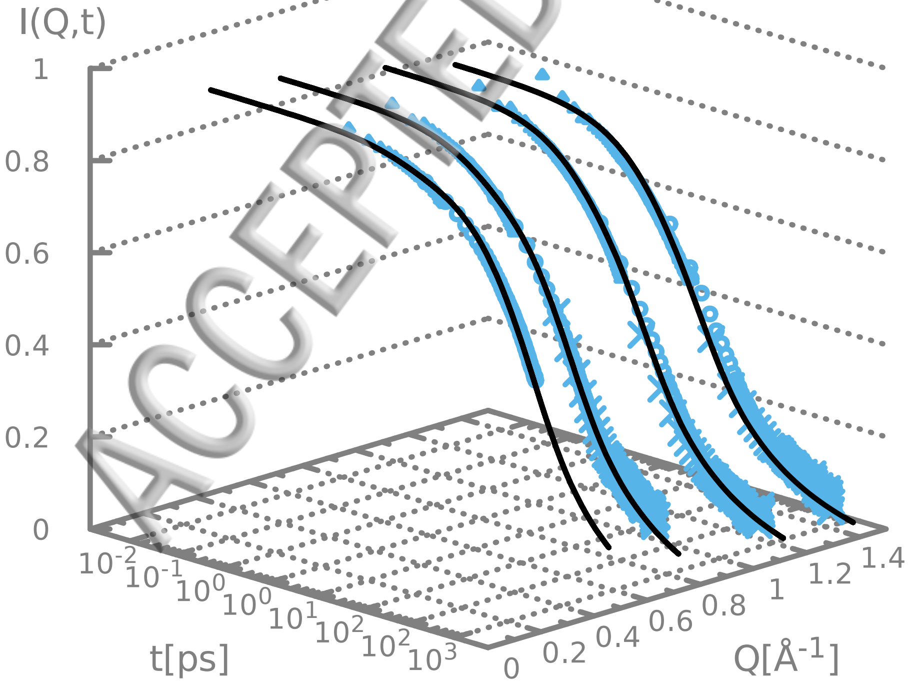
I(Q,t)
1
0.8
0.6
0.4
0.2
0
$10^{-2}$
$10^{-1}$
$10^{0}$
$10^{0}$
$10^{1}$
$10^{2}$
$10^{2}$
$10^{3}$
t[ps]
0
0.2
0.4
0.6
0.8
1
1.2
1.4
Q[Å$^{-1}$]

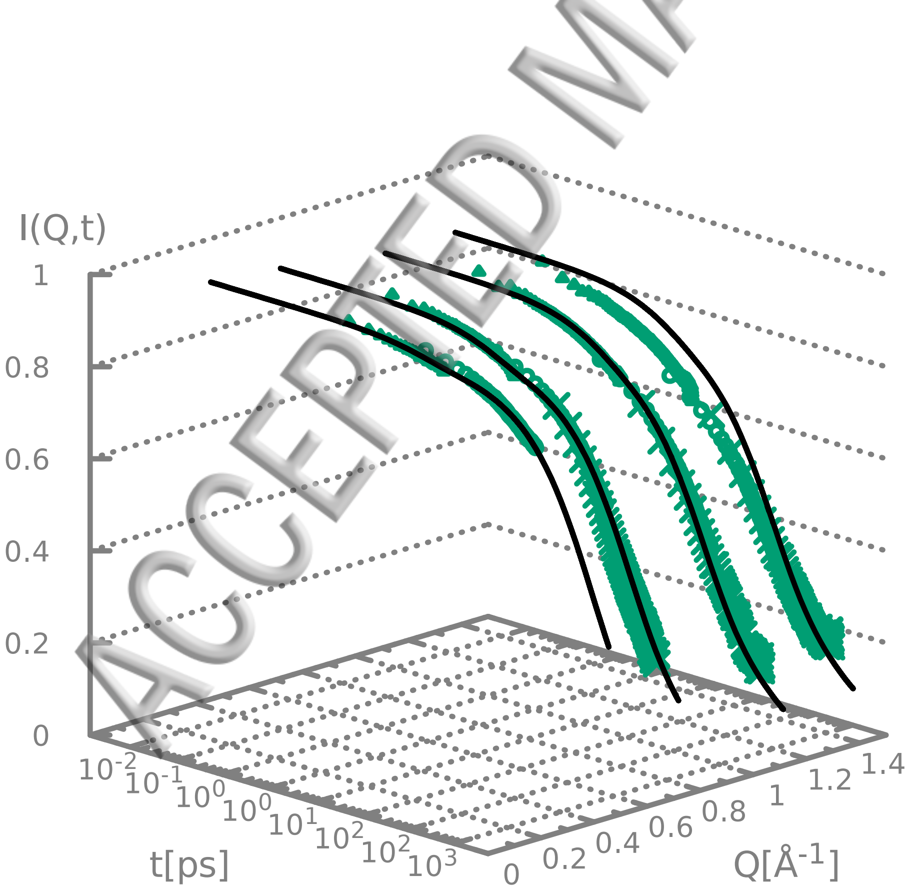
I(Q,t)
1
0.8
0.6
0.4
0.2
0
$10^{-2}$
$10^{-1}$
$10^{0}$
$10^{0}$
$10^{1}$
$10^{2}$
$10^{2}$
$10^{3}$
t[ps]
0
0.2
0.4
0.6
0.8
1
1.2
1.4
Q[Å$^{-1}$]

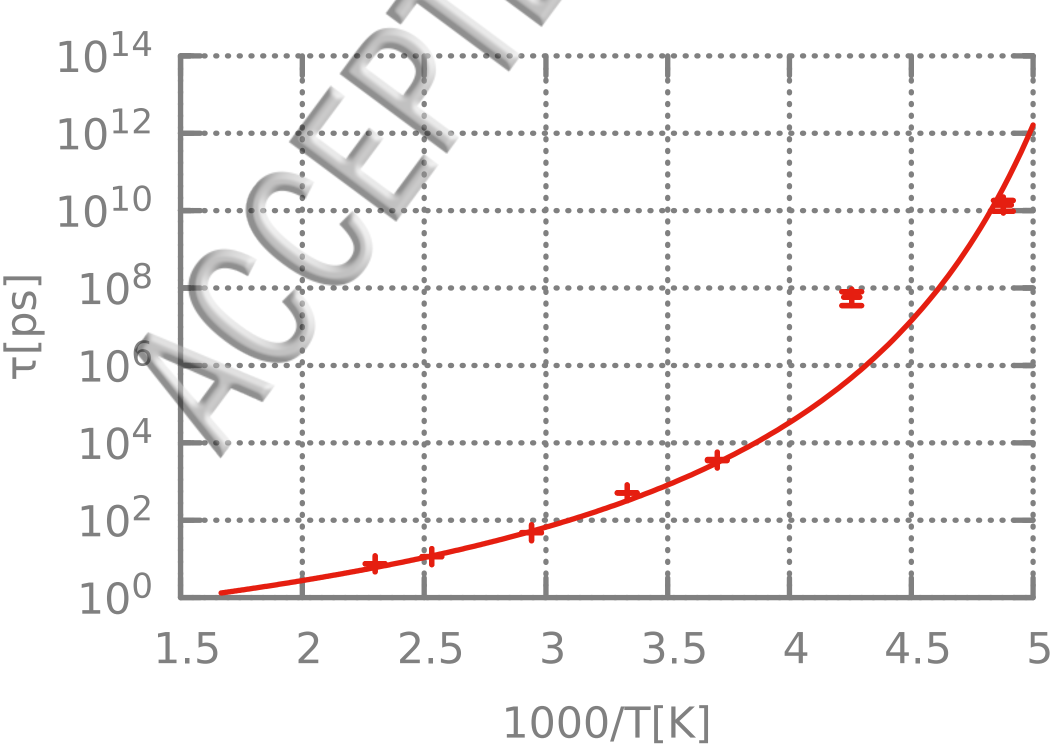
$10^{14}$
$10^{12}$
$10^{10}$
$10^{8}$
$10^{6}$
$10^{4}$
$10^{2}$
$10^{0}$
τ[ps]
1.5
2
2.5
3
3.5
4
4.5
5
1000/T[K]

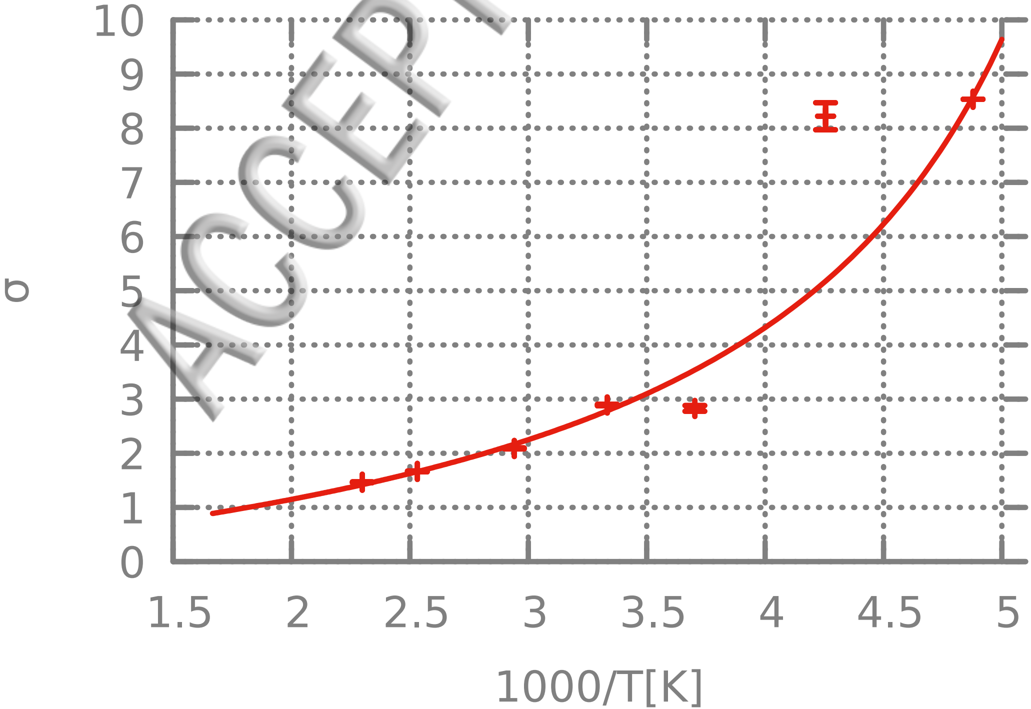
σ
0
1
2
3
4
5
6
7
8
9
10
1.5
2
2.5
3
3.5
4
4.5
5
1000/T[K]

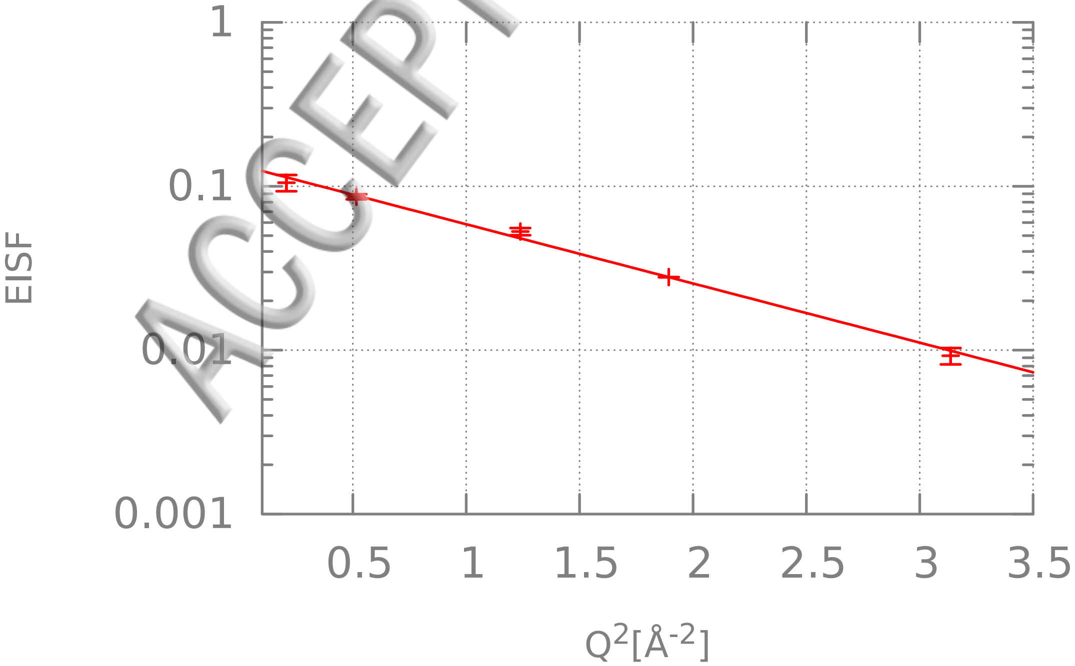
EISF
1
0.1
0.01
0.001
0.5
1
1.5
2
2.5
3
3.5
$Q^2$[$Å^{-2}$]

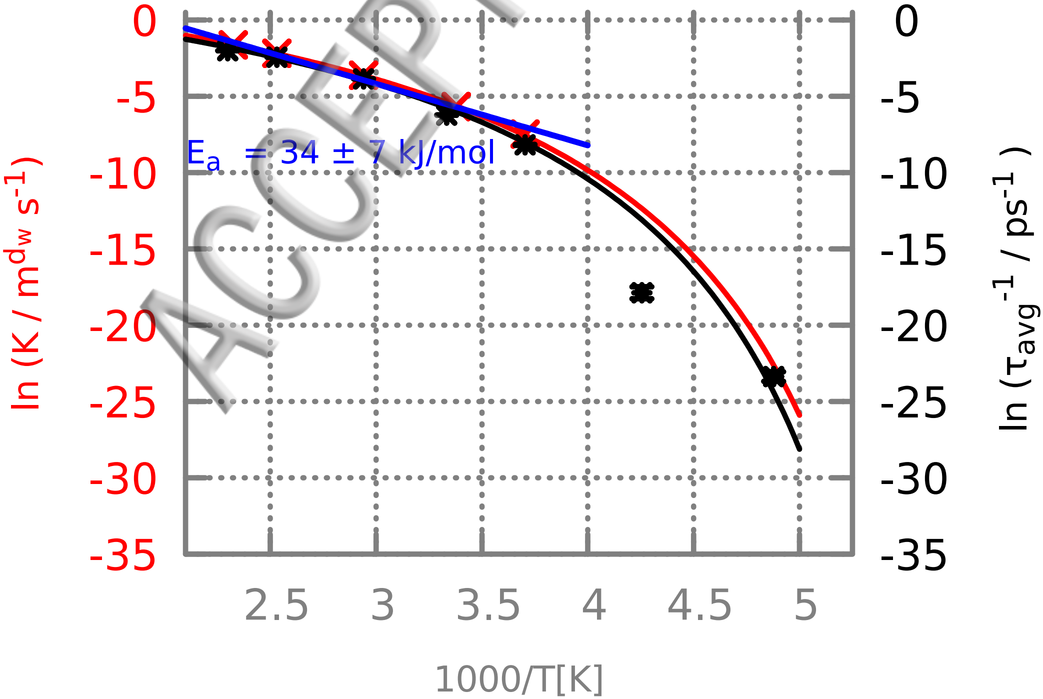
0
-5
-10
-15
-20
-25
-30
-35
ln (K / m$^{d_w}$ s$^{-1}$)
0
-5
-10
-15
-20
-25
-30
-35
ln ($\tau_{avg}^{-1}$ / ps$^{-1}$ )
$E_a$ = 34 ± 7 kJ/mol
2.5
3
3.5
4
4.5
5
1000/T[K]